Supporting Information

All-day freshwater and power generation via integrated photothermal-enhanced thermoelectrics and evaporation cooling

Wenhe Zhang,‡[a] Chengbing Wang,*‡[a] Lu Wang,[a] Fan Wang,[a] Puxin Tan,[a] Jinchi Ma,[a] Jingjing Jin,[a] Zhongrong Geng,*[b] Hongyao Xie,*[c] and Li-Dong Zhao*[c]

[a] School of Materials Science and Engineering, Shaanxi Key Laboratory of Green Preparation and Functionalization for Inorganic Material, Shaanxi University of Science & Technology, Xi'an, Shaanxi 710021, China

[b] School of Materials Science and Engineering, Lanzhou Jiaotong University, Lanzhou, 730070, China

[c] School of Materials Science and Engineering, Beihang University, Beijing, 100191, China

‡ These Authors contributed equally to the work: Wenhe Zhang, Chengbing Wang.

*Corresponding authors: wangcb@sust.edu.cn (C. Wang), gengzhongrong@lzjtu.edu.cn (Z. Geng), xiehongyao@buaa.edu.cn (H. Xie), zhaolidong@buaa.edu.cn (L-D. Zhao)

Section 1. Supplementary Notes

Section 2. Supplementary Figures

Section 1. Supplementary Notes

Note S1 Calculation of selective absorption performance of AATO LEA

The solar absorptance (α) and thermal emittance (ε) are determined from the reflectance spectra using the following formulas:[1]

$$\alpha = \int_{300nm}^{2500nm} \frac{I_s(\lambda)(1 - R(\lambda))d\lambda}{I_s(\lambda)d\lambda} \quad \text{(S1)}$$

$$\varepsilon = \int_{2.5\mu m}^{25\mu m} \frac{I_b(\lambda,T)(1 - R(\lambda))d\lambda}{I_b(\lambda,T)d\lambda} \quad \text{(S2)}$$

$$I_b(\lambda,T) = \frac{C_1}{\lambda^5 \times [e^{C_2/(\lambda T)} - 1]} \quad \text{(S3)}$$

Where λ is the wavelength, $R(\lambda)$ represents the measured reflectance spectra of the coating, $I_s(\lambda)$ is the AM 1.5 solar spectral radiation defined by ISO standard 9845–1(1992), $I_b(\lambda, T)$ is the black body radiation at temperature T according to Planck's law, C_1=3.743×10^{-16} W m^2, and C_2=1.4387×10^{-2} m K.

Note S2 Calculation of water evaporation rate of ACPFG

The water evaporation rate (v) is calculated using the following equation:

$$v = \frac{m}{St} \tag{S6}$$

Where m represents the mass loss during evaporation in kg, S represents the area of the sample (projected area) in m^2, and t represents the evaporation time in h.

Note S3 The water collection rate of ACPFG

Regarding the water collection rate (W_c)[2]

$$W_c = \frac{m}{A\cos\theta t} \quad \text{(S7)}$$

Among them, m refers to the mass of water collected within time t (unit: h), in kg, and A refers to the area of water collection (0.003025 m^2), θ (45˚) refers to the angle at which the TEG is tilted.

Note S4 Quantitative comparison of water-electricity cogeneration capacity

Regarding the four works related to water-electricity cogeneration in Table 1, in order to comprehensively analyze who has the best comprehensive ability, we used a weighted scoring method for quantitative analysis. Firstly, assuming that the importance of electricity production and water production is equal, a weight of 0.5 can be assigned to electricity production (w_1) and water production (w_2) respectively.

Next, normalize each indicator. Due to the different numerical ranges and units of electricity and water production, in order to make them comparable, it is necessary to normalize these two indicators. The linear normalization method is used here, and the formula is:

$$X_{norm} = \frac{X - X_{min}}{X_{max} - X_{min}} \quad \text{(S8)}$$

Among them, X_{norm} is the normalized value. X is the original value of electricity (or water) production. X_{min} is the minimum value in electricity (or water) production, and X_{max} is the maximum value in electricity (or water) production.

Normalization of power generation ($P_{max\text{-}norm}$): The power generation data are 1.726 W m^{-2}, 0.47 W m^{-2}, 0.63 W m^{-2} and 1.349 W m^{-2}. Among them, X_{min} is 0.47 W m^{-2}, and X_{max} is 1.349 W m^{-2}. Calculate the normalized value (X_{norm1}) of electricity production according to equation (S8).

Water production normalization ($W_{c\text{-}norm}$): The water production data is 0.067 kg m^{-2} h^{-1}, 1.02 kg m^{-2} h^{-1}, 1.2 kg m^{-2} h^{-1} and 0.986 kg m^{-2} h^{-1}. Among them, X_{min} is 0.067 kg m^{-2} h^{-1}, and X_{max} is 1.2 kg m^{-2} h^{-1}. Calculate the normalized value (X_{norm2}) of the produced water according to equation (S8).

Finally, calculate the comprehensive capacity of water-electricity cogeneration. According to the following formula:

$$S = w_1 \times X_{norm1} + w_2 \times X_{norm2}$$

Table S1 The table of quantitative comparison of water-electricity cogeneration capacity

Materials	P_{max} ($W\ m^{-2}$)	W_c ($kg\ m^{-2}\ h^{-1}$)	$P_{max\text{-}norm}$ (X_{norm1})	$W_{c\text{-}norm}$ (X_{norm2})	Normalization (S)	Ref.
Dual-functional coating layer	1.726	0.067	1	0	0.5	[3]
MWCNT/PDA layer	0.47	1.02	0	0.841	0.4205	[4]
PXF–90/TE	0.63	1.2	0.127	1	0.5635	[5]
AATO–ACPFG	1.349	0.986	0.700	0.811	0.7555	This work

By comparing the comprehensive capacity of water-electricity cogeneration, it was found that ACPFG had the highest comprehensive score. This indicates that when the importance of electricity and water production is equal (with a weight of 0.5), ACPFG has the best water-electricity cogeneration.

Note S5 Calculation of energy exchange in ACPFG

Calculate the energy utilization efficiency of ACPFG through the law of energy balance, which means that the total sum of energy input and output inside ACPFG remains balanced. To simplify the calculation process, we made a reasonable assumption by ignoring lateral heat loss (including internal lateral heat loss from LEA and TEG), and focusing mainly on the heat loss at the hot end of LEA and the heat loss on the evaporation side[6]. The energy exchange process of ACPFG during operation is calculated as follows:

Initial energy input to the hot end (P_{input}):

$$P_{input} = P_{solar} - P'_{r,LEA'} - P'_{rad,LEA'} - P'_{conv,LEA'}$$

Among them, P_{solar} is the solar energy absorbed by LEA:

$$P_{solar} = C_{opt} \times I \times S_{LEA}$$

Where C_{opt} is the optical concentration, I is intensity of direct insolation on the horizontally cross-sectional plane of the absorber (1 kW m^{-2}), and S_{LEA} is the area of the whole LEA. And $P'_{r, LEA'}$ is the solar reflection loss of excess LEA that does not cover TEG (LEA'):

$$P'_{r,LEA'} = r \times P_{solar}$$

where r is the reflectivity of LEA;

$P'_{rad, LEA'}$ is the radiative heat loss of LEA':

$$P'_{rad,LEA'} = S'_{LEA'} \varepsilon_{LEA} \sigma (T_{LEA}^{4} - T_{amb}^{4})$$

where ε_{LEA} is the thermal emissivity of the LEA, σ is the Stefan-Boltzmann constant (5.67×10^{-8} W m^{-2} K^{-4}), T_{LEA} is the surface temperature of the LEA, T_{amb} is the ambient temperature. And $S'_{LEA'}$ is the area of the LEA':

$$S'_{LEA'} = S_A - S_{TEG}$$

S_A is the entire area of LEA, and S_{TEG} represents the area of TEG;

$P'_{conv, LEA'}$ is the convective heat loss of the LEA':

$$P'_{conv,LEA'} = S_{LEA'} h (T_{LEA} - T_{amb})$$

where h is the coefficient of thermal convection;

Further calculate the solar reflection loss ($P_{r, LEA}$) of LEA covering TEG:

$$P_{r,LEA} = r \times P_{solar} - P'_{r,LEA'}$$

The heat loss at the hot end (P_h)

Hot end heat loss composed of radiative heat loss ($P_{rad, h}$) and convective heat loss ($P_{conv, h}$)

$$P_h = P_{rad,h} + P_{conv,h}$$

$$P_{rad,h} = S_{LEA}\varepsilon_{LEA}\sigma(T_{LEA}^4 - T_{amb}^4)$$

$$P_{conv,h} = S_{LEA}h(T_{LEA} - T_{amb})$$

Among them: S_{LEA}=S_{TEG}, i.e., the area of the LEA that covers the TEG;

The heat loss at the cold end (P_c)

Cold end heat loss composed of radiative heat loss ($P_{rad, c}$) and convective heat loss ($P_{conv,c}$)

$$P_c = P_{rad,c} + P_{conv,c}$$

$$P_{rad,c} = S_{TEG}\varepsilon_c\sigma(T_c^4 - T_{amb}^4)$$

$$P_{conv,c} = S_{TEG}h(T_c - T_{amb})$$

Where, ε_c is the thermal emissivity of the cold end material, T_c is the surface temperature of the cold end, and T_{amb} is the temperature of the ambient temperature.

Energy consumption of TEG thermoelectric conversion (P_e):

$$P_e = P_{out} \times S_{TEG}$$

Where P_{out} is the output power density during the power generation process;

Therefore, the energy lost (P_l) in ACPFG is:

$$P_l = P_{r,LEA} + P_h + P_c + P_e$$

The energy utilization rate (η) is:

$$\eta = \frac{P_{input} - P_l}{P_{input}} \times 100\%$$

Calculations show that the energy utilization rate of ACPFGs are above 86.9% (Table S1).

It should be noted that many factors such as environmental conditions, light intensity, TEG specifications, and component compatibility can affect heat transfer, making it difficult to accurately calculate some numerical results. The figures are only a reference result. However, the above calculations can be used to qualitatively propose the optimal direction for the co-production of electricity and water by solar heating and water evaporation cooling. For example, (1) solar energy absorption can be increased by reducing the reflectivity of LEA; (2) Reduce the emissivity of LEA, decrease radiative heat dissipation, and increase heat input to the hot end; (3) Improving the matching degree of system components, especially reducing the air gap between components, is beneficial for improving convective heat transfer and water evaporation. (4) In addition, the power generation efficiency of the system depends on a large temperature difference, so theoretically, thermoelectric modules with better performance under the same conditions are more conducive to outputting thermoelectric performance, which is closely related to their preparation process, specifications and models.

Note S6 A preliminary estimation of the cost for ACPFG and its payback period

We have made a preliminary estimate of the material cost of the ACPFG system and the payback period under real conditions. The ACPFG system demonstrates economic feasibility for off-grid deployment but faces a long payback period due to industry bottlenecks. However, it holds investment prospects through advancing thermoelectric materials and adapting to water- and power-scarce scenarios. The specific analyses are shown below:

(1) Manufacturing cost of a single ACPFG system:

The system consists of LEA, TEG, and CAT components, where the LEA consists of an Al substrate and an Ag/Al–TiO_2 coating.

(I) The cost of the Al substrate is calculated based on the area: we purchased the Al sheet (50 cm × 20 cm) at a cost of 18 RMB, so the prices of A5.5 (5.5 cm × 5.5 cm), A7.5 (7.5 cm × 8.5 cm), A10 (10 cm × 12 cm), and A13 (13 cm × 13 cm) Al sheets are the product of the corresponding area and the unit purchase cost of Al sheets.

(II) The cost of Ag/Al–TiO_2 coating mainly includes the consumption of target materials (Ag, Al, TiO_2) and Ar gas. Since four sizes of LEAs, A5.5, A7.5, A10 and A13, can be prepared in the same batch in the same chamber, the cost of individual LEAs is calculated based on the cost of materials consumed in a single preparation. The specific costing basis for each material is shown in Table S2.

(III) Individual system CAT cost: It costs a total of 42.5 RMB to purchase 100 CATs measuring 22 × 22 cm^2, and a uniform 22 × 5.5 cm^2 size CAT is required in each system. Therefore, the individual CAT cost is calculated by the product of the individual CAT area and the cost of purchasing per unit area.

(IV) The remaining fixed material cost: one TEG costs 25 RMB. Each water supply-collection device costs 4 RMB.

(V) The cost of each material in the ACPFG system is shown in Table S3:

Table S2 Detailed breakdown of single coating preparation cost based on target cost and consumption

Materials for manufacture	Specification	Procurement cost (RMB)	Total preparation times (Times)	Single preparation cost (RMB)	Single preparation total cost (RMB)	Single coating cost (RMB)
Ag target	1 piece	1000	50	20	28.5	7.13
Al target	1 piece	200	50	4		
TiO_2 target	1 piece	750	500	1.5		
Ar gas	1 bottle	150	50	3		

Table S3 Material cost for a single ACPFG system

Materials	Unit	A5.5-ACPFG	A7.5-ACPFG	A10-ACPFG	A13-ACPFG
Al substrate	RMB	0.54	1.15	2.16	3.04
Materials for manufacture	RMB	7.13	7.13	7.13	7.13
TEG	RMB	25	25	25	25
CAT	RMB	1.06	1.06	1.06	1.06
Water supply-collection device	RMB	4	4	4	4
Total	RMB	37.73	38.34	39.35	40.23
	USD	5.24	5.33	5.47	5.59

1 USD = 7.2 RMB

(2) Initial one-time fixed investment (per m^2)

As indicated in Table S3, the material cost of a single ACPFG system lies within the range of 5.25 ~5.59 USD, which demonstrates an exceptionally low cost. Given the relatively minor cost differences among the options, and considering the overall production capacity as a pivotal factor (where the A13-ACPFG system exhibits the best performance), we choose the A13-ACPFG system for the investment payback calculation. The plan is to place 35 sets of A13-ACPFG systems per m^2 based on the total footprint of a single A13-ACPFG system (0.018 m×0.013 m). So, further calculation:

(I) Material cost: 40.23 RMB × 35;

(II) Manufacturing cost: 200 RMB/m^2 + 2 RMB/system × 35;

(III) Transportation cost: 2 RMB/kg × 0.2kg/system× 35;

(IV) Land rent: one-time payment, shared at 3000 RMB per mu (1 mu = 666 m^2);

(V) Installation cost: one-time payment, shared at 3000 RMB per mu;

(VI) Total preliminary costs (per m^2) = Material cost + Manufacturing cost + Transportation cost+ Land rent + Installation cost

Based on the above, the detailed one-time fixed investment cost of 35 sets of A13-ACPFG system per m^2 is calculated as shown in Table S4:

Table S4 Cost breakdown of upfront one-time fixed investment of 35 sets of A13-ACPFG systems per m^2

	Unit	Cost
Material Cost	RMB	1408.05
Manufacturing Cost	RMB	270
Transport Cost	RMB	14
Venue rent	RMB	4.5
Installation Cost	RMB	4.5
Total preliminary costs	RMB	1701.05
	USD	236.26

(3) Calculation of income items (per m^2/year)

(I) Electricity generation revenue

Assuming a daily effective temperature difference duration of 12 hours (ignoring nighttime work), calculate the annual power generation per m^2 based on the output power density (1.349 W/m^2), and the revenue is 1.5 RMB/kWh;

(II) Water production revenue

Assuming a daily effective water production of 12 hours (ignoring nighttime work), calculate the annual water collection per m^2 based on a water collection rate (0.986 kg/m^2/h), with a revenue of 5 RMB/ton;

(III) Annual operation and maintenance cost

Assuming one worker is responsible for 10 mu of land per year, with an annual salary of 20000 RMB;

(IV) Annual net income = Electricity production revenue + Water production revenue - Annual operation and maintenance cost. The specific details are shown in Table S5.

(4) Calculation of investment payback period

Investment payback period (year) = Annual net income/Total preliminary costs, as shown in Table S5:

Table S5 Annual revenue per m^2 with payback period

	Production	Unit price	Profit	
Electricity production	5.91 kWh/year	1.5 RMB/ kWh	8.87 RMB/ year	1.23 USD/ year
Water production	4.32 tons/year	5 RMB/ton	21.60 RMB/ year	3.00 USD/ year
Annual operation and maintenance costs	-	-	3.00 RMB/ year	0.42 USD/ year
Annual net income	-	-	27.47 RMB/ year	3.81 USD/ year
Payback	-	-	61.94 year	61.94 year

From the above analysis, it is found that the ACPFG system demonstrates significant low-cost advantages, with ultra-low material costs per unit (max \$5.59). Core components (Al substrate, TEG, CAT) feature commercially controllable costs (Tables S2, S3). For scaled deployment (35 units/m^2), material costs dominate upfront fixed investments at 82.7% (\$236.26, Table S4), highlighting its core competitiveness in ultra-low material costs. This lays a critical cost foundation for initial commercial deployment in off-grid scenarios.

Although the ACPFG system shows significant low-cost advantages, it has a long payback period if actually deployed today (Table S5). This stems from inherent limitations of commercial TEG materials ($ZT \approx 1$): their power density lags far behind photovoltaics under low temperature differences,[7-9] and constrained water collection area (i. e, TEG area) restricts water production capacity. This reflects an industry-wide challenge, not our system design flaw. ACPFG's differentiation value lies in being the first 24 h water-electricity cogeneration system via synergistic LEA-enhanced solar absorption and passive evaporative cooling, deployable in water-scarce/off-grid regions. Future advances in TEG materials (e.g. $ZT > 2$) that can significantly increase power output, as well as optimization of the system structure (e.g. enlarging the area of the TEGs, increasing the condensation efficiency of the catchment chambers to increase the amount of water collected) can significantly reduce the payback period. Therefore, our work validates ultra-low costs and technical viability under current

conditions, providing a scalable framework for future high-performance thermoelectric materials.

Section 2. Supplementary Figures

S2.1 Preparation and characterization of AATO LEA

We deposited multi-layered Ag/Al–TiO_2 (AATO) LEAs with typical dual absorption layer metal-ceramic structure[10] by magnetron sputtering for photothermal conversion (Fig. S1a1). From bottom to top (Fig.S1a2), Ag layer and Al layer are infrared reflectors to reduce infrared heat loss; Al–doped TiO_2 with high metal content and Al–doped TiO_2 with low metal content work together as double absorption layer to increase the absorption of sunlight. And the outermost layer is an anti-reflection layer to reduce the reflection of sunlight reaching the absorber. It is found from the physical figure that AATO LEAs shows a uniform dark blue color and SEM shows that its surface is composed of uniformly sized nanoparticles (Fig. S1b) and the EDS surface scanning was performed, revealing a uniform distribution of Ag, Al, Ti, and O elements. And the cross-sectional SEM shows that overall coating thickness is only 820 nm (Fig. S1c).

XRD characterization (Fig. S1d) shows that the peaks appeared at $2\theta = 38.2°$, 44.4°, 64.44° and 77.38°, respectively. According to the PDF card, they represent Al (111), Al (220) (PDF#85–1327) and Ag (220), Ag (311) (PDF#87–0717). No obvious peaks related to titanium oxide were observed, mainly due to the coverage of peaks from the strong metal layer. Further analyze the elemental composition and structure of AATO LEA through XPS (Fig. S1e). The Ag 3d orbit is mainly divided into peaks with a core of 368.3 eV and 374.3 eV, corresponding to Ag 3d 5/2 and Ag 3d 3/2, respectively. The Al 2p orbital observes peak with 72.9 eV as the core, corresponding to and metallic Al. The Ti 2p orbital contains energy levels centered at 458.4 eV and 464.2 eV, corresponding to Ti 2p 1/2 and Ti 2p 3/2 of Ti^{4+}, respectively. Analyzing the O 1s orbital, there are mainly peaks centered around 530.0 eV and 531.5 eV, corresponding to TiO_2 and Al_2O_3, respectively.

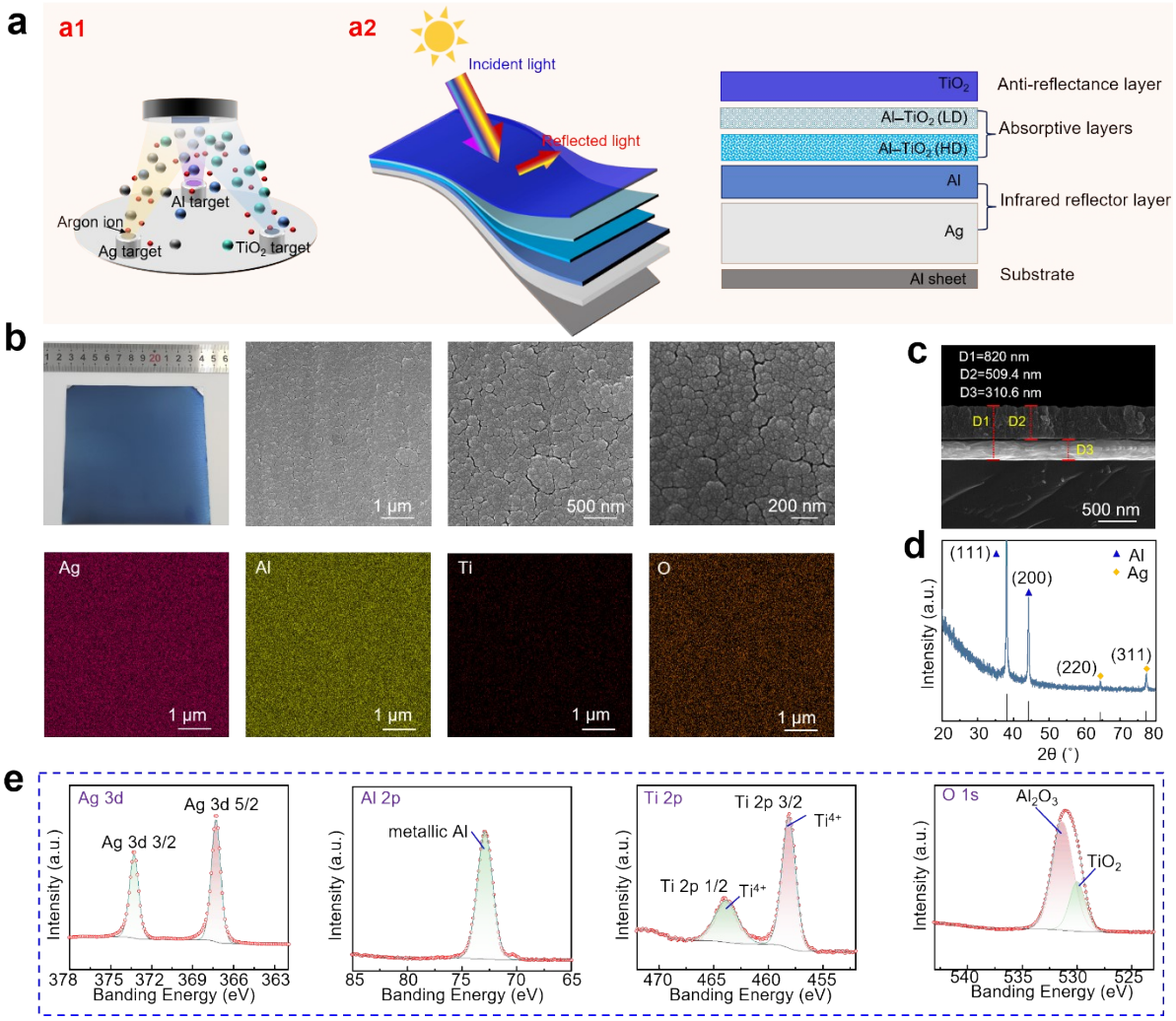

Fig. S1 Preparation and characterization of AATO LEA. (a) Preparation of AATO LEA by magnetron sputtering with Ag, Al and TiO_2 targets (a1). Composition and structure of AATO LEA (a2). From bottom to top, the Al substrate, Al layer and Ag layer together serve as the infrared reflection layer, dual absorption layer doped with TiO_2 with different Al contents, and TiO_2 anti-reflection layer. (b) Physical image, SEM and EDS surface scanning images of AATO LEA. The (c) cross-sectional SEM and (d) XRD patterns and (e) XPS spectra of Ag, Al, Ti, and O elements of AATO LEA.

S2.2 The photothermal conversion performance of AATO LEA

It is found that its surface temperature could reach 56.6 ℃ and 90.6 ℃ after being irradiated for 420 s under the 0.5 and 1.0 sun, respectively. Besides, it exhibited rapid light response ability and stable photothermal conversion performance in the cycling experiment of the on/off light (Fig. S2a). It can be clearly seen that the temperature gradually increased from the corresponding infrared photos taken at different times (Fig. S2b, c).

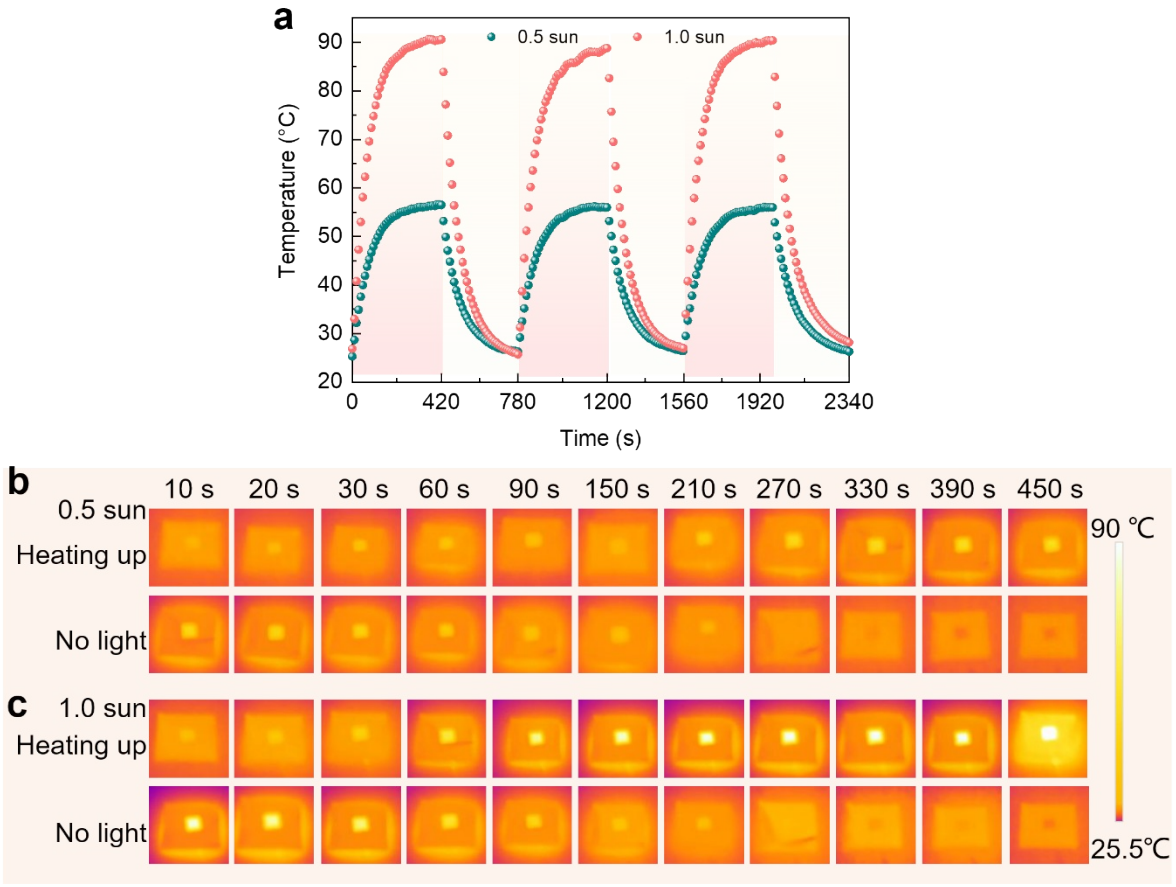

Fig. S2 The photothermal conversion performance of AATO LEA. (a) The variation of Al/ATO LEA surface temperature over time under the 0.5 and 1.0 sun indoors. The infrared photographs of Al/ATO LEA under the (b) 0.5 sun and (c) 1.0 sun indoors.

S2.3 The ability to transport water of CAT

For materials with superhydrophilicity at the cold end, the CAT can be selected. The dynamic contact angle is shown in Fig. S3a, and it is found that only 70 ms were used from the beginning of the water droplet contacting the CAT to been absorbed completely. In order to visually display its water absorption, the CAT with a width of 5.5 cm was extended into the blue-black ink contained in a glass dish for a length of 0.3 mm (Fig. S3b), and it is found that it can quickly transport water only under the action of capillary force. After 10 seconds, the water absorption height is 2 cm, and after 120 s, it can reach 6 cm. Therefore, its strong water-absorbing ability due to its superhydrophilic properties and the action of capillary force has a unique advantage during the water evaporation cooling.

The thickness of the original CAT was 0.4 mm. Based on this, we further studied the cases with thicknesses of 0.8 mm and 1.2 mm. Under the same solar intensity, keeping the LEA at the hot end unchanged and only replacing CAT with different thicknesses at the cold end, a 20 min thermoelectric output experiment was conducted.

The experimental results show that as the thickness of CAT increases, the temperature at the cold end of the device gradually decreases (Fig. S3c). On the contrary, the temperature difference (ΔT) of TEG increases continuously with the increase of CAT thickness (Fig. S3d), and correspondingly, its open-circuit voltage (V_{oc}) also increases in sequence (Fig. S3e). When water flows through the TEG cold end, waste heat will cause water to evaporate, and the evaporated water vapor is easily condensed on the side wall of the device near the water flow channel. We observed that as the thickness of CAT increased, the number of water droplets condensed on the side walls of the device gradually decreased (Fig. S3f). Therefore, it can be seen that increasing the thickness of CAT helps to improve thermoelectric output, but it will

reduce the ability to produce water. The main reason is that as the thickness of CAT increases, the flow rate of water passing through the cold end accelerates, causing the temperature at the cold end to decrease and thus increasing the temperature difference to improve thermoelectric output. However, the decrease in cold end temperature will lead to a decrease in the evaporation rate of water, ultimately resulting in a reduction in the amount of collected water.

Based on analysis and observed (Fig. S3d and S3f), we found that the impact of CAT thickness on water production capacity is much greater than its impact on thermoelectric output. So, in order to pursue comprehensive water-electricity cogeneration capacity, a 0.4 mm CAT should be chosen.

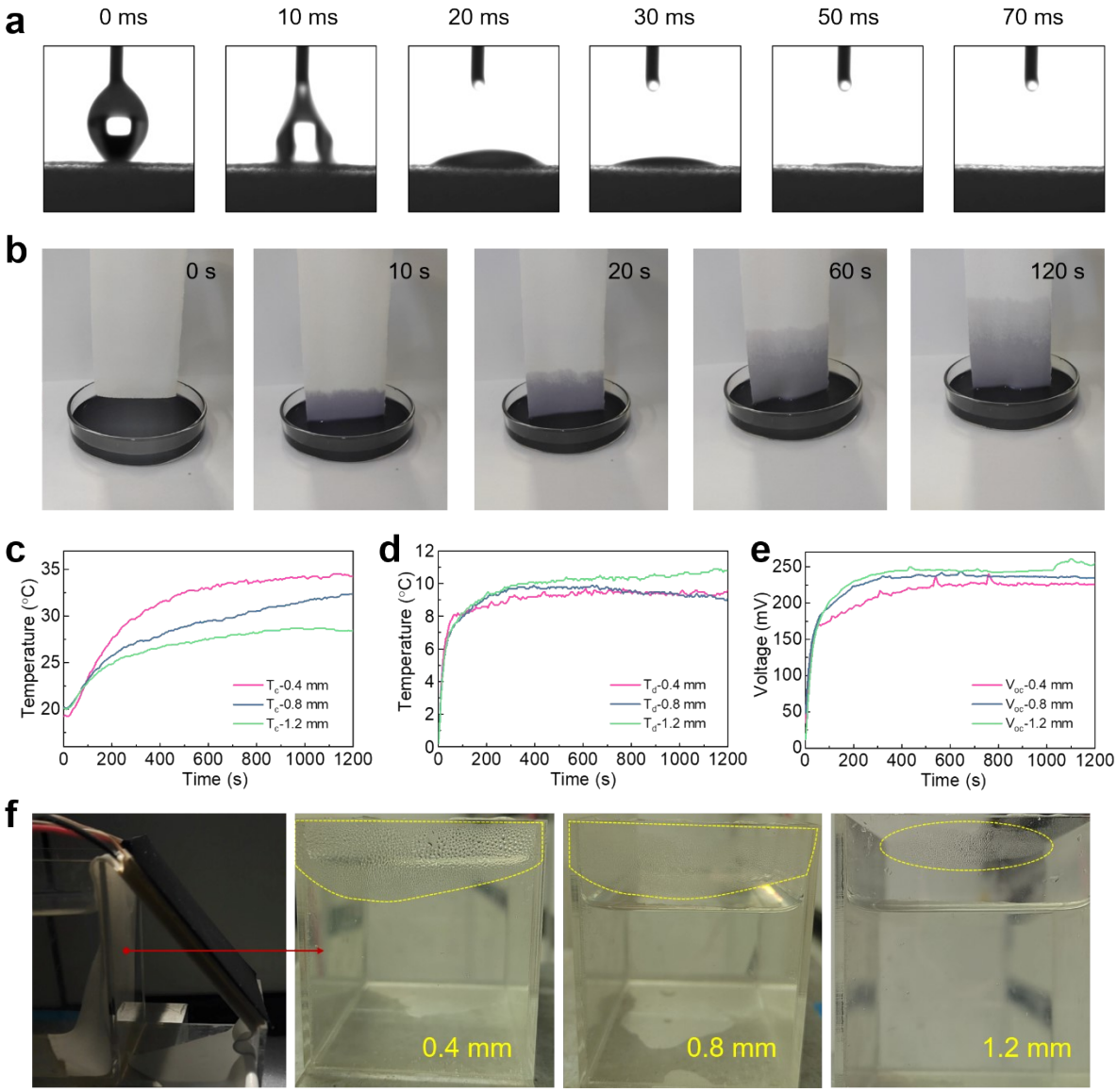

Fig. S3 The ability to transport water of CAT. (a) The dynamic contact angle of CAT. (b) The CAT with a width of 5.5 cm was extended into the blue-black ink contained in a glass dish to absorb water. Under the same solar intensity, the effects of CAT with different thicknesses (0.4 mm, 0.8 mm, and 1.2 mm) on the (c) cold end temperature, (d) temperature difference, and (e) open-circuit voltage of TEG, as well as (f) corresponding photos of the water evaporating from the cold end and condensing into water droplets on the sidewall of device after 20 min of operation.

S2.4 The thermoelectric output of control experiments

The core components of the ACPFG system are, from top to bottom, a LEA, a TEG and a CAT (Fig. S4a). These components are connected through a thermal conductive tape, which is made of fiberglass material with a thickness of only 0.15 mm and a thermal conductivity coefficient of 1.5 W/ (m·K). In addition, the tape exhibits excellent mechanical properties: a 180 ° peel strength of over 14 N/25 mm and an initial adhesion force of 1.4 kg/inch, ensuring a tight fit between components. Its working temperature range is wide, and it can maintain stable performance from -20 ℃ to 120 ℃. These data clearly reveal that the thermal conductive tape we selected can significantly improve the thermal conductivity efficiency of ACPFG due to its ultra-thin thickness and high thermal conductivity. And its strong bonding ability with the components ensures stable connection of key components such as TEG, LEA and CAT, effectively preventing possible loosening or separation of components during operation.

In terms of temperature measurement, in order to accurately obtain key temperature parameters that directly affect the output power of TEG, we placed thermocouple contacts on the hot end surface of TEG, followed by thermal conductive tape and solar absorber, as shown in the physical images in Fig. S4b. Therefore, the hot side temperature mentioned in the article specifically refers to the temperature of the TEG hot end. This setting aims to accurately monitor the temperature changes of the TEG hot end throughout the entire system operation process, providing accurate data support for evaluating and analyzing the thermoelectric performance of the system.

The performance of STEG exhibits significant differences under different thermal management strategies (Fig. S4c). Specifically, under 1.0 sun indoors, when relying solely on PFW cooling (SP), the hot end temperature only reaches 30.1 ℃, with a ΔT of only 3.75 ℃,

and the generated V_{oc} is 63 mV (Fig. S4d). In contrast, if only AATO LEA solar heating method is used (SL), the hot end temperature significantly increases to 55.3 ℃, the ΔT expands to 6.08 ℃, and the V_{oc} also increases to 138.6 mV (Fig. S4e). When the two are applied in combination (ACPFG, III), the hot end temperature drops to 45.9 ℃ (Fig. S4f). The T_h, T_c and T_d when SP, SL, and ACPFG reach stability within 1 hour, and their maximum V_{oc} reached are shown in Fig. S4g. ACPFG exhibited the best performance, which can be attributed to the effective effect of evaporative cooling using PFW at the cold end, which timely takes away some heat and further reduces the hot end temperature. It is important to note that this temperature decrease did not weaken the ΔT (instead increased to 9 ℃), significantly enhancing the system's thermoelectric output, manifested as a significant increase in V_{oc} (from 128.7 mV to 238.9 mV). Therefore, the design that combines the two not only effectively reduces heat loss, but also achieves higher thermoelectric output by optimizing thermal management strategies.

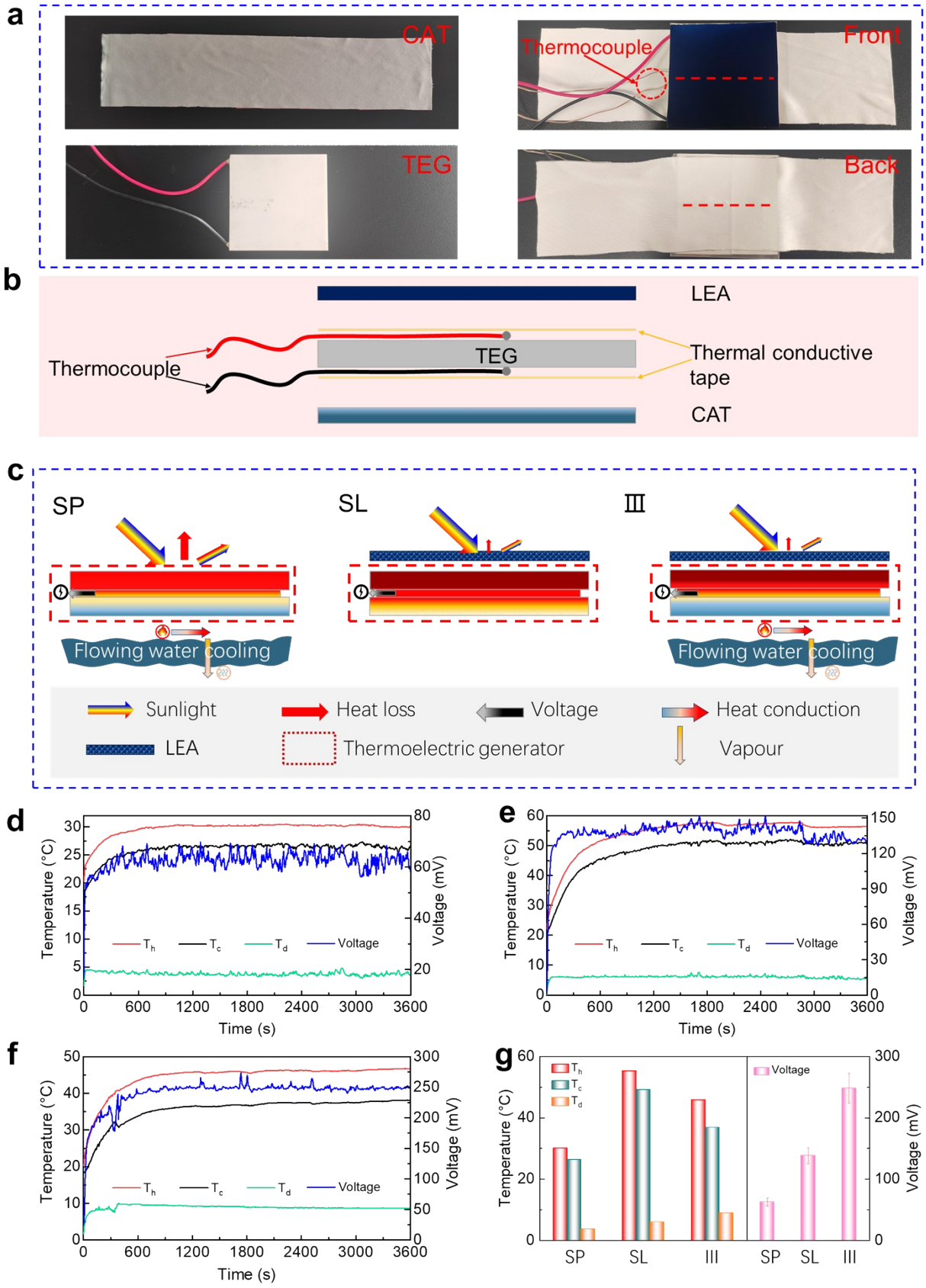

Fig. S4 (a) Physical photos of CAT and TEG, as well as front and back photos of the core of the ACPFG system composed of LEA, TEG, and CAT. (b) The cross-sectional diagram along

the red dashed line shown in (a) shows LEA, thermal conductive tape, thermocouple, TEG, thermocouple, thermal conductive tape, and CAT from top to bottom. (c) Temperature distribution diagrams of STEG using only PFW evaporation cooling (SP), STEG using only AATO LEA solar heating (SL), and STEG integrating AATO LEA solar heating and PFW evaporation cooling (III, ACPFG). The change in T_h, T_c, T_d and V_{oc} of (d) SP, (e) SL, and (f) ACPFG within 1 hour under 1.0 sun. (g) The T_h, T_c and T_d when SP, SL, and ACPFG reach stability within 1 hour, and their maximum V_{oc} reached.

S2.5 The impact of different cold end configurations on TE performance

When the cold end is a heat sink (I), the hot end temperature reaches 70.4 ℃, with a ΔT of 6.99 ℃, and the V_{oc} is 201.3 mV (Fig. S5a); When the cold end is replaced with static water (II), the temperature of the hot end drops to 56.9 ℃, but the ΔT to 7.93 ℃, and the V_{oc} also increases to 237.5 mV (Fig. S5b); Most notably, when PFW is used at the cold end (III, ACPFG), the temperature at the hot end further decreases to 45.9 ℃, but the ΔT expands to the highest of 9 ℃, and the V_{oc} also reaches the highest of 248.3 mV (Fig. S5c).

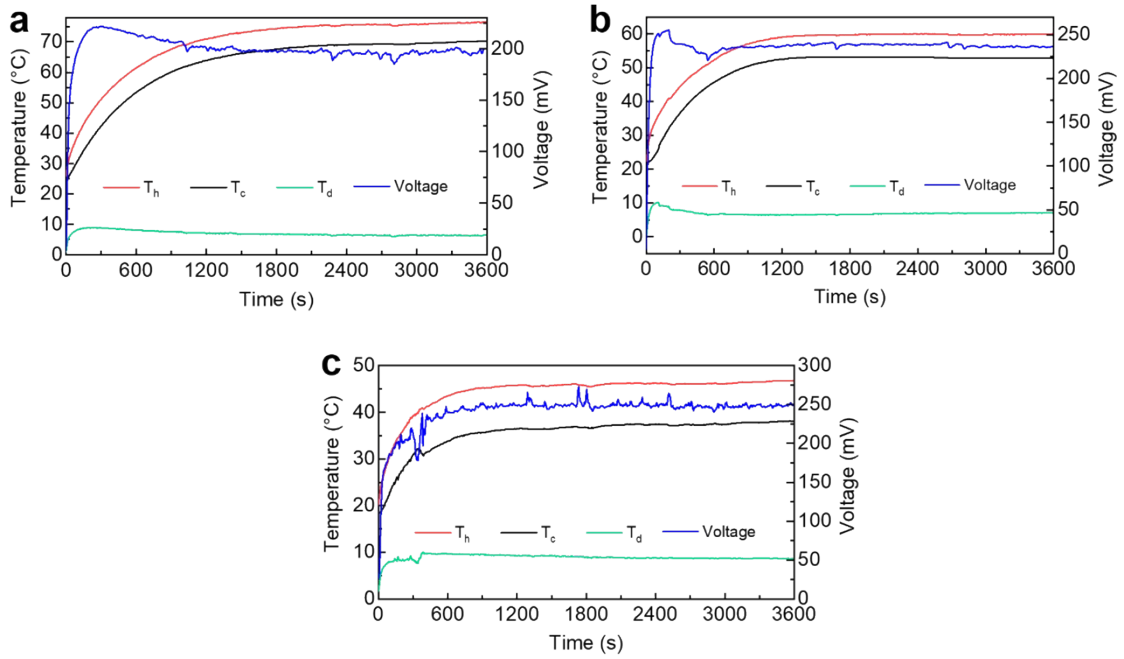

Fig. S5 The change of T_h, T_c, T_d and V_{oc} of STEG with both AATO LEA solar heating and (a) heat sink cooling (I) or (b) static bulk water cooling (II) or (c)PFW evaporation cooling (III, ACPFG) within 1 hour under 1.0 sun.

S2.6 The temperature distribution of STEG and ACPFG

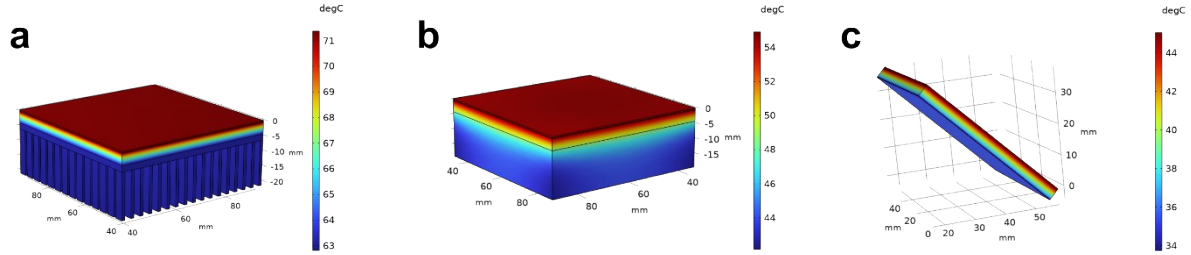

Fig. S6 Multi physics simulation of surface temperature distribution of STEG and ACPFG. The temperature distribution of (a) STEG with both AATO LEA solar heating and heat sink cooling (I), (b) STEG with both AATO LEA solar heating and bulk water cooling (II), as well as (c) STEG with both AATO LEA solar heating and PFW evaporation cooling (III, ACPFG) under 1.0 sun. The simulation results show that the temperature difference of ACPFG is significantly larger than that of I and II, and the overall temperature is lower, indicating that flowing water cooling can significantly improve the performance of STEG and reduce thermal radiation loss.

S2.7 The photothermal conversion performance of AATO LEA–TEG

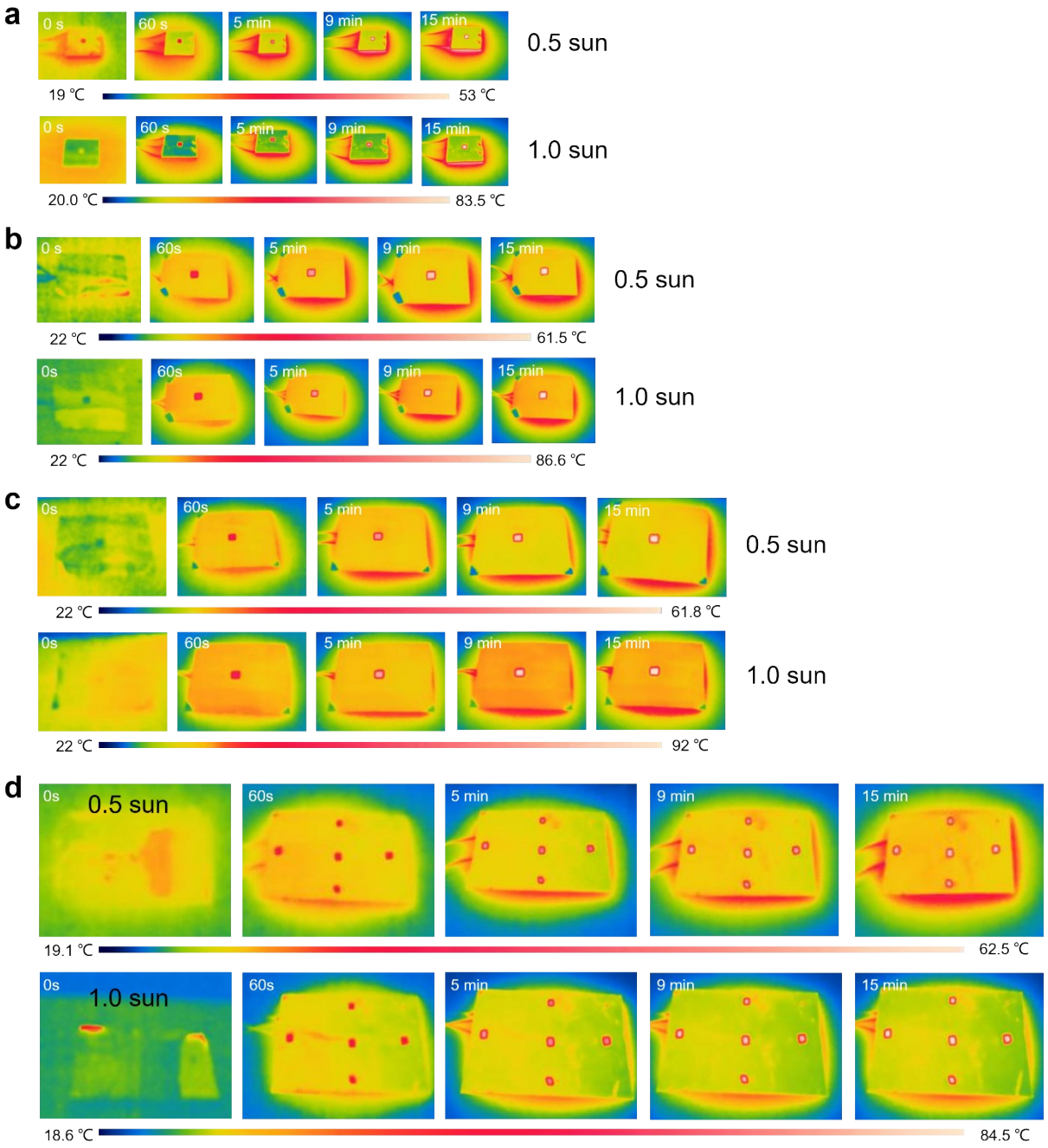

Fig. S7 Infrared photos of the AATO LEA surface at different times of indoor exposure to 0.5 and 1.0 sunlight for (a) A5.5, (b) A7.5, (c) A10, and (d) A13.

S2.8 Temperature changes of ACPFG before and after feedwater outdoors

On July 26, 2024, A5.5, A7.5, A10, and A13–ACPFG were placed together in an open area at Shaanxi University of Science and Technology in Xi'an, China, and their temperature changes at the cold and hot ends were measured before and after feeding water to the cold end. The cold end temperatures were measured by multi-channel thermocouples (Fig. S8a) and the hot end temperatures were measured by infrared camera (Fig. S8b–d). Before water supply (10:36 ~ 13:20), the ACPFG showed an immediate and rapid increase in cold-end temperature from exposure to sunlight (initial cold-end temperatures of 36.8, 39.1, 40.3, and 41 ℃) to 53.1, 55.8, 57.4, and 62.9 ℃ after 10 min (Fig. S8a), respectively. After that, their cold-end temperatures increased with the enhancement of sunlight intensity, reaching 55.2, 60.4, 61.6 and 64.8 ℃ at 13:00 (Fig. S8a), while the corresponding hot-end temperatures were 57.3, 61.4, 65 and 67.1 ℃, respectively (Fig. S8b, c). The experimental results indicate that when heated solely by natural light outdoors, an increase in the area of AATO LEA is beneficial for raising the temperature.

The water supply for A5.5, A7.5, A10, and A13–ACPFG was started at 13:20 (Fig. S8a). After the water flowed through the cold end of the TEG, it was found that the cold end temperature rapidly decreased and then stabilized at around 37.1, 39.0, 42.8, and 44.2 ℃ (Fig. S8a). For the hot end temperatures, they were 43.4, 48.1, 52.3, and 54.1 ℃ at 14:30, respectively and were 35.1, 38.0, 39.6, and 40.7 ℃ at 17:00 (Fig. S8b, c), respectively. The results showed that the temperature at the cold and hot ends decreased significantly after water supply, mainly because when water flows in the cold end, it not only carries heat through convective heat transfer, but also absorbs latent heat through evaporation. These two mechanisms work together to significantly improve the heat dissipation effect at the cold end. Due to the enhanced heat dissipation capability of the cold end, the temperature difference between the hot and cold ends further increases. In order to reach thermal equilibrium again,

the hot end will transfer more heat to the cold end. However, due to the efficient heat dissipation capability of the cold end (including convective heat transfer and evaporative cooling), this heat is quickly carried away, resulting in a decrease in temperature at both the hot and cold ends.

When the ACPFG continues to work until evening (at 20:00), it is found that the surroundings are already pitch black from the illustration in the upper left corner of Fig. S8b. At this time, the cold end temperatures of A5.5, A7.5, A10, and A13–ACPFG are 28.7, 29.1, 29.4, and 29.9 ℃ (Fig. S8a), respectively, and the corresponding hot end temperatures are 29.1, 29.4, 30.3, and 30.7 ℃ (Fig. S8b, c), respectively. This indicates that the cold end temperature is still lower than the hot end temperature at night when there is no sunlight, i.e., there is a temperature difference, explaining why the thermoelectric output still exists at night.

In addition, the Fig. S8d displays the infrared photos (around 2:30 pm) of the temperature on the side and back of TEG during the cold end process of water flow passing through A5.5, A7.5, A10, and A13–ACPFG, which intuitively indicates that under the condition of a constant temperature of the feedwater (40 ℃), as the AATO LEA area increases, the corresponding temperature at the cold end will also increase, which further indirectly indicates that increasing the LEA area is beneficial for improving the temperature of photothermal conversion.

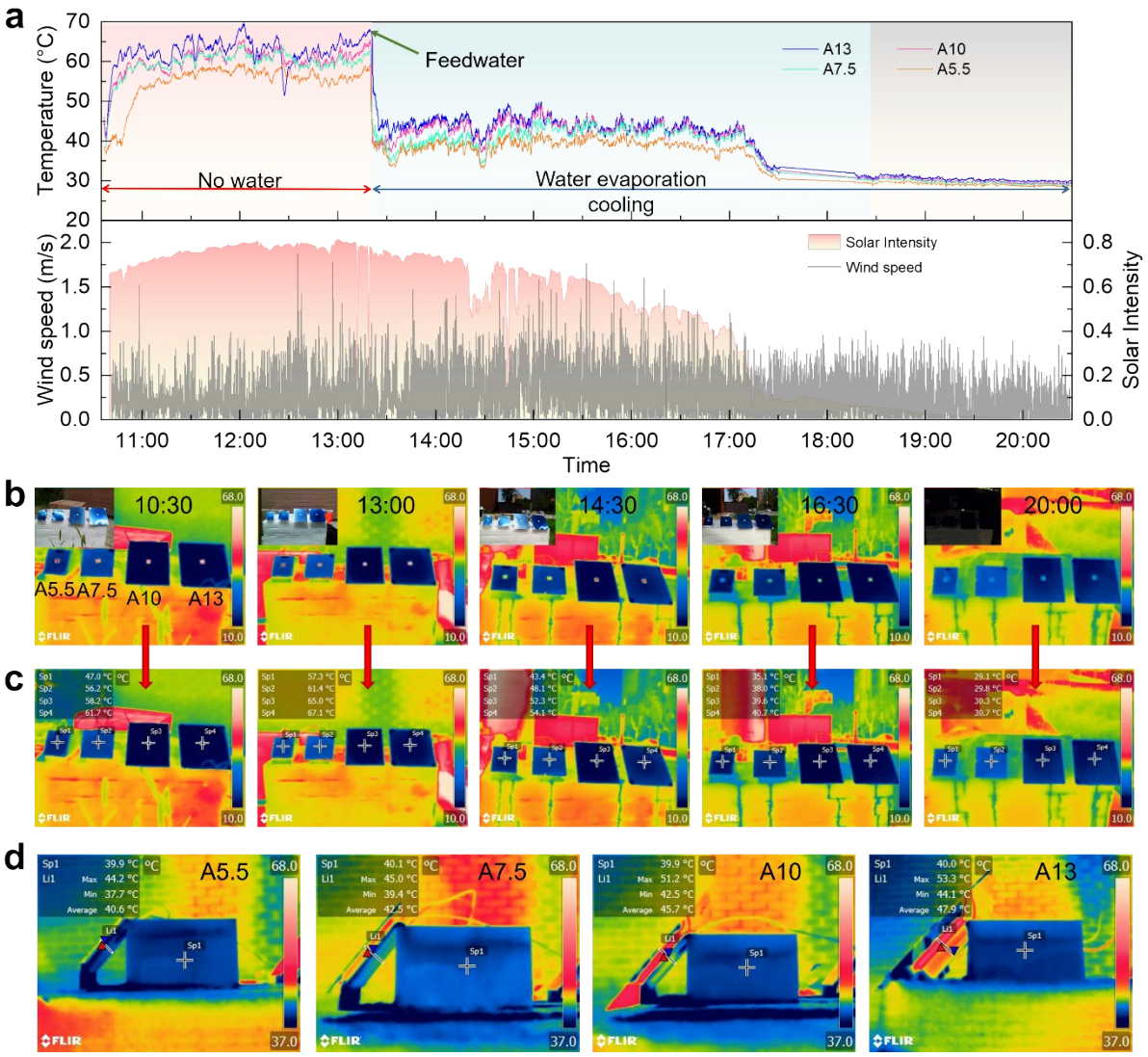

Fig. S8 (a) The change in TEG cold end temperature of ACPFG in the absence (10:36 ~ 13:20) and presence (13:20 ~ 20:30) of flowing water-cooling outdoors. And changes in outdoor solar intensity and wind speed. In the sunny weather, the wind speed is between 0–1.8 m/s. Infrared photos taken by ACPFG at different time periods outdoors: (b) The center of the adhesive tape with high thermal emissivity (>0.9) displays its highest temperature, and the embedded image in the upper left corner is the corresponding physical image, which is at 10:40, 13:00, 14:30, 17:00, and 20:00, respectively. (c) The corresponding temperature coordinates and values of the adhesive tape, and (d) The infrared photo of ACPFG on the side during the cooling process by flowing water (around 2:30 pm), can clearly show the back temperature of the TEG.

S2.9 The thermoelectric output of ACPFG under 1.0 sun

The over-sized AATO LEAs have greater solar heating capacity to further improve the thermoelectric output of ACPFGs. Under 1.0 sun, the hot end temperatures of A5.5, A7.5, A10, and A13 reached 45.9, 47.1, 52.3, and 57.4 ℃, respectively, with ΔTs of 9, 9.7, 10.8, and 13.9 ℃, resulting in V_{oc} of 248.3, 284.6, 353 and 445 mV, respectively.

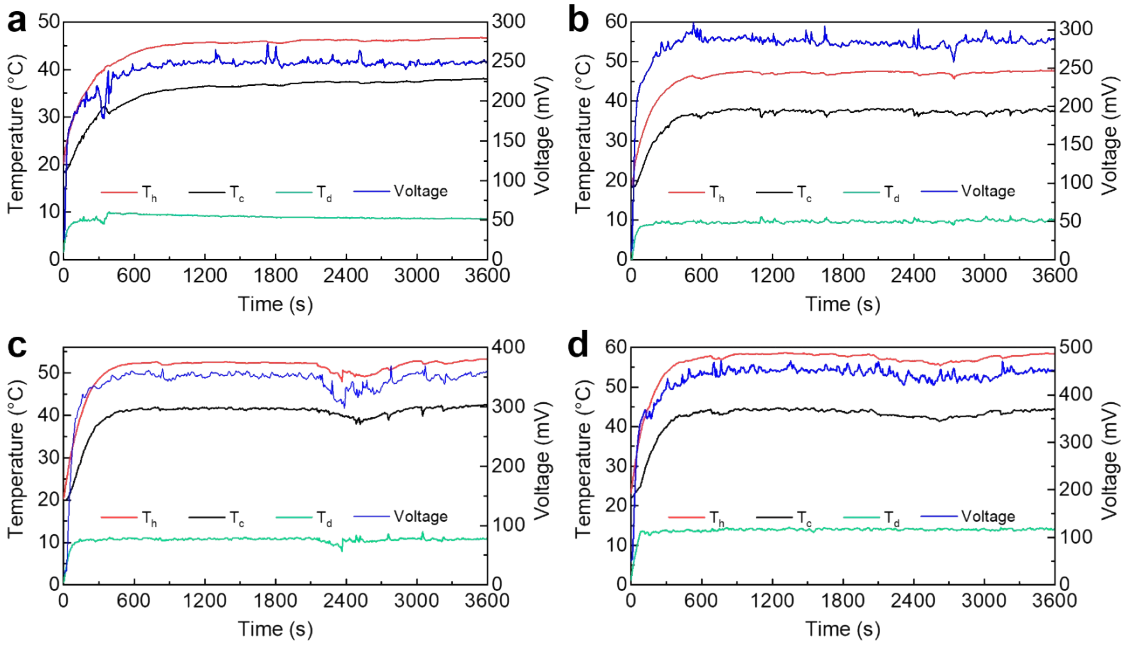

Fig. S9 The change of T_h, T_c, T_d and V_{oc} within 1 hour under 1.0 sun of the ACPFG. (a) A5.5, i.e., STEG integrated AATO LEA solar heating and PFW evaporation cooling mentioned above (III), (b) A7.5, (c) A10, and (d) A13

S2.10 The thermoelectric output of ACPFG under high solar intensity

Under 1.5 sun, the hot end temperatures of A5.5, A7.5, A10, and A13 reached 50.4, 57.1, 58.1, and 52.5 ℃, respectively, with ΔTs of 11.9, 14.4, 14.5, and 12.5 ℃, resulting in average V_{oc} of 308.3, 400.7, 414.8 and 347.6 mV (Fig. S10), respectively.

Under 2.0 sun, the hot end temperatures of A5.5, A7.5, A10, and A13 reached 59, 68.1, 67, and 61.7 ℃, respectively, with ΔTs of 14.2, 18.4, 18.6, and 15.7 ℃, resulting in average V_{oc} of 438.9, 541.3, 531.7 and 457.7 mV, respectively (Fig. S11).

Therefore, if only the change in solar intensity is considered, the V_{oc} of A5.5, A7.5, and A10 all increase with the increase of solar intensity. However, in terms of considering the increasing LEA area, the thermoelectric output is significantly improved under 1.0 sun (Fig. S8). But under 1.5 and 2.0 sun, the V_{oc} showed a trend of first increasing and then decreasing, mainly due to the increase in light intensity and the decrease in aperture area under the limitation of indoor simulated light intensity, which resulted in local radiation around LEA being unable to reach, leading to heat loss.

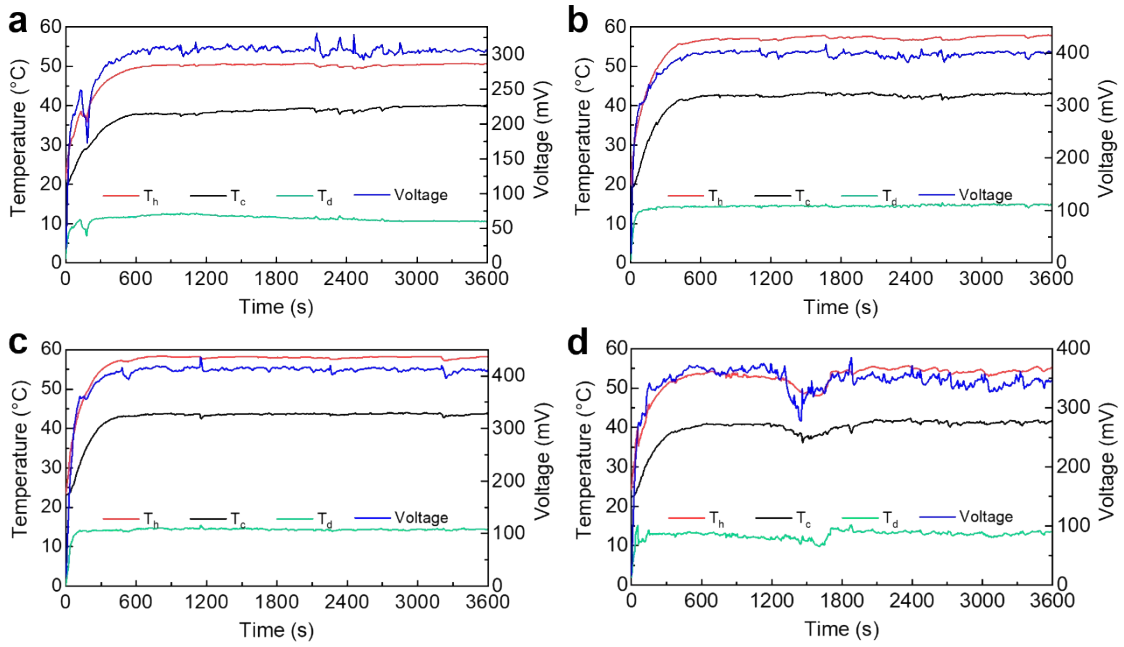

Fig. S10 The change of T_h, T_c, T_d and V_{oc} within 1 hour under 1.5 sun of the ACPFG. (a) A5.5, (b) A7.5, (c) A10, and (d) A13.

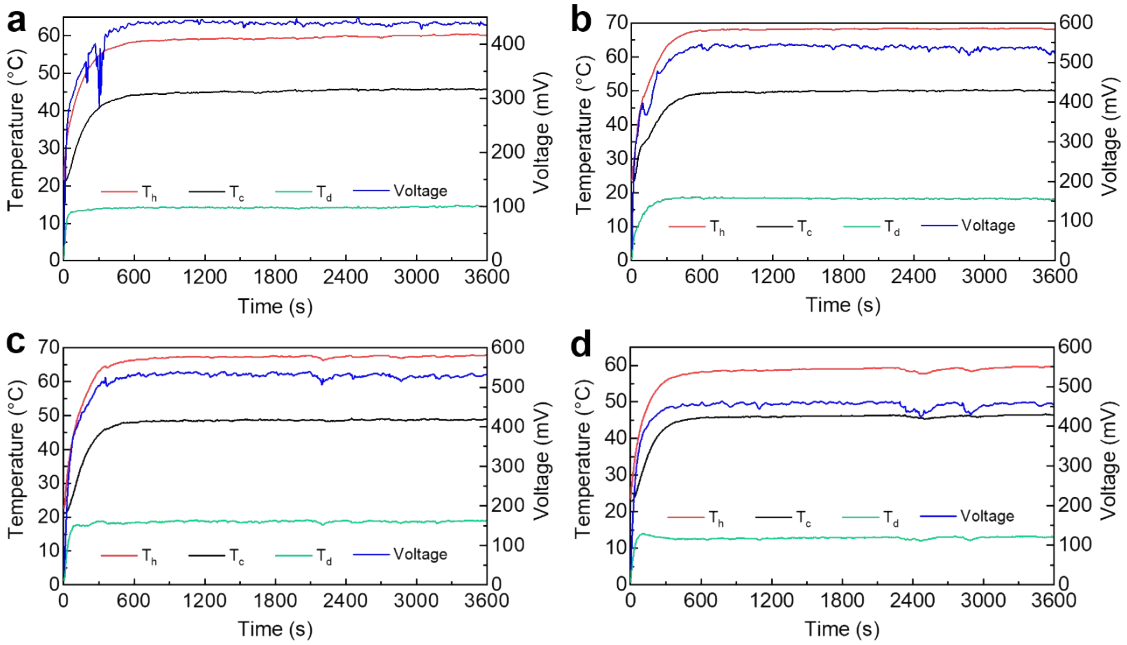

Fig. S11 The change of T_h, T_c, T_d and V_{oc} within 1 hour under 2.0 sun of the ACPFG. (a) A5.5, (b) A7.5, (c) A10, and (d) A13.

S2.11 Water evaporation performance of ACPFG

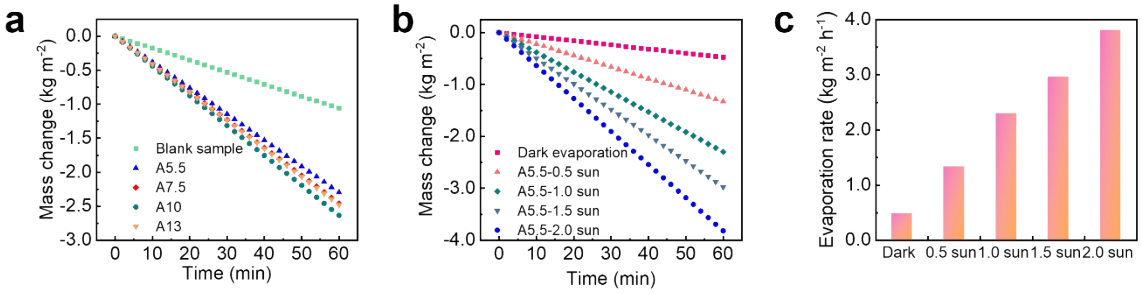

Fig. S12 (a) The change in evaporation mass of blank samples (pure TEG surface), A5.5, A7.5, A10, and A13–ACPFG in 3.5 wt% simulated seawater under 1.0 sun. The change in evaporation mass (b) and (c) evaporation rates of A5.5–ACPFG in 3.5 wt% simulated seawater under no sunlight, 0.5 sun, 1.0 sun, 1.5 sun, and 2.0 sun, respectively.

S2.12 Water purification capability of ACPFG

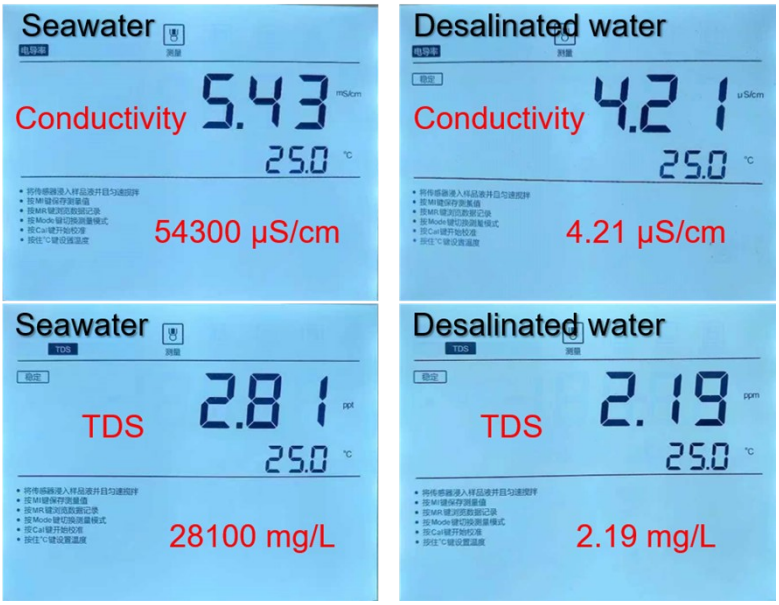

Fig. S13 Comparison of conductivity and TDS measured by Water Quality Tester between 3.5 wt% simulated seawater and the water collected by ACPFG.

S2.13 The thermoelectric device of ACPFG during water collection

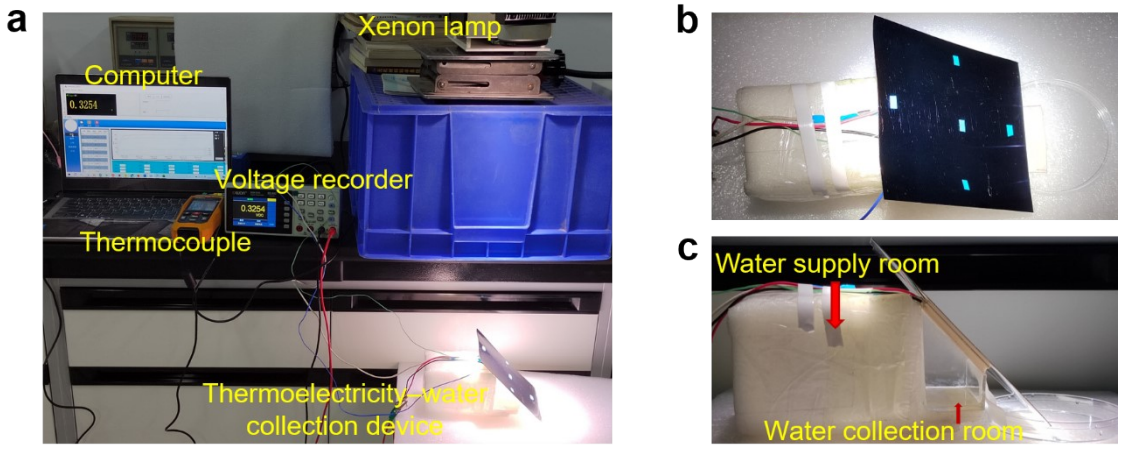

Fig. S14 A display of ACPFG working indoors. (a) Schematic diagram of the thermoelectricity-water collection device under simulated sunlight indoors. The computer is used to record in real-time the temperature of the cold and hot ends measured by thermocouples and the voltage measured by voltage recorders. (b) Top view of and (c) side view of thermoelectricity-water collection device illuminated by sunlight.

S2.14 The thermoelectric output of ACPFG during water collection in pure water

Regarding the thermoelectric output capability of ACPFG during collecting water. Pure water was used for evaporation cooling under 1.0 sun. For A5.5, the hot end temperature was 52.9 ℃ and the ΔT was 8.1 ℃, resulting in the average V_{oc} of 225.1 mV (Fig. S15a). For A7.5, the hot end temperature was 51.6 ℃ and the ΔT reached 8.7 ℃, resulting in the average V_{oc} of 256.8 mV (Fig. S15b). For A10, the hot end temperature was 56.7 ℃ and the ΔT reached 9.6 ℃, resulting in the average V_{oc} of 277.2 mV (Fig. S15c). For A13, the hot end temperature was 62 ℃ and the ΔT reached 12.7 ℃, resulting in the average V_{oc} of 368.2 mV (Fig. S15d). And the T_h, T_c and T_d when A5.5, A7.5, A10, and A13–ACPFG reach stability within 1 hour, and their maximum V_{oc} reached are shown in Fig. S15e. It is obvious that the V_{oc} of A13 is highest than that of all others, still demonstrating that ACPFG can show superior performance by simply increasing the LEA area at natural light intensities without relying on spotlighting or other additional light enhancement techniques.

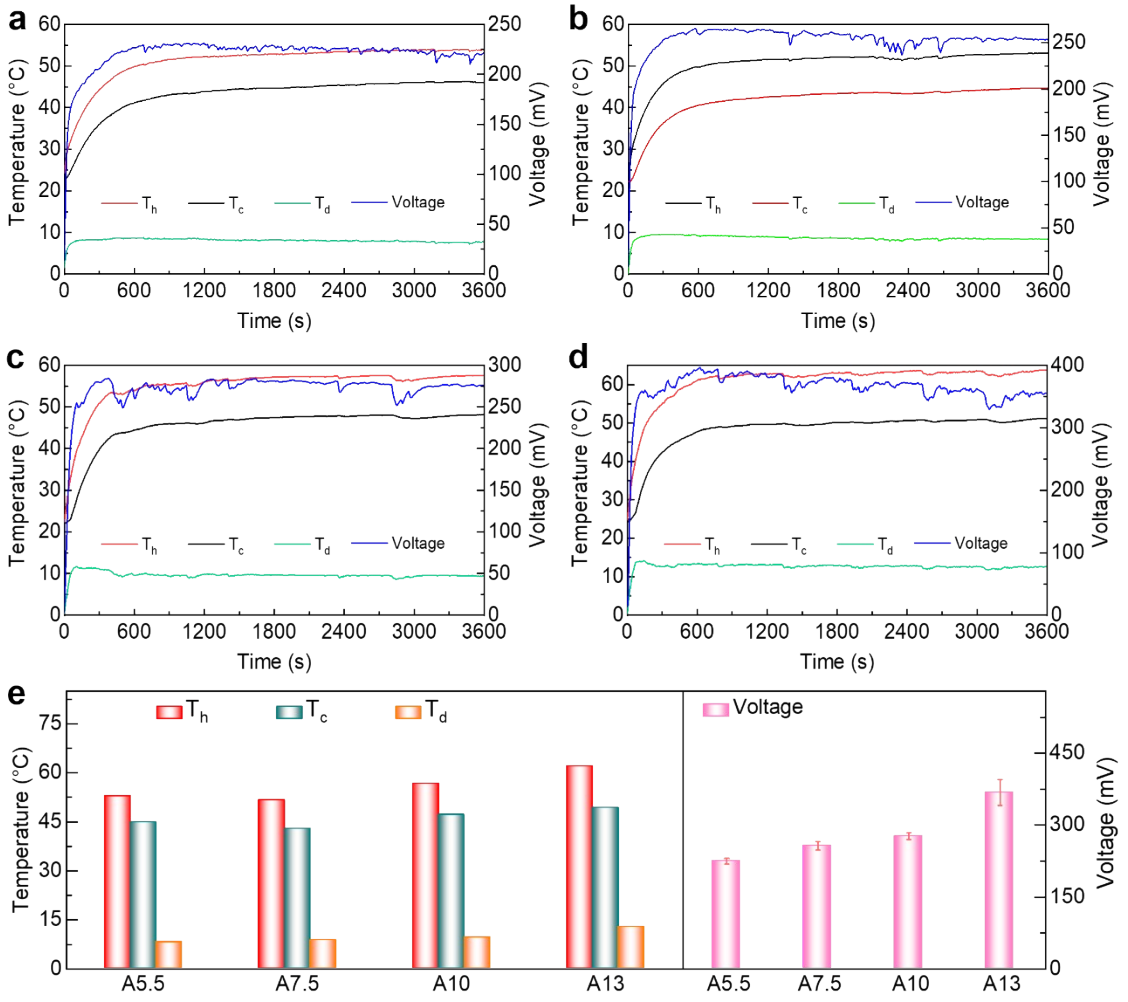

Fig. S15 The change of T_h, T_c, T_d and V_{oc} within 1 hour under 1.0 sun during water collection by ACPFG. (a) A5.5, (b) A7.5, (c) A10, and (d) A13. e, The T_h, T_c and T_d when A5.5, A7.5, A10, and A13–ACPFG reach stability within 1 hour, and their maximum V_{oc} reached.

S2.15 The thermoelectric output of A5.5–ACPFG during water collection in NaCl solutions

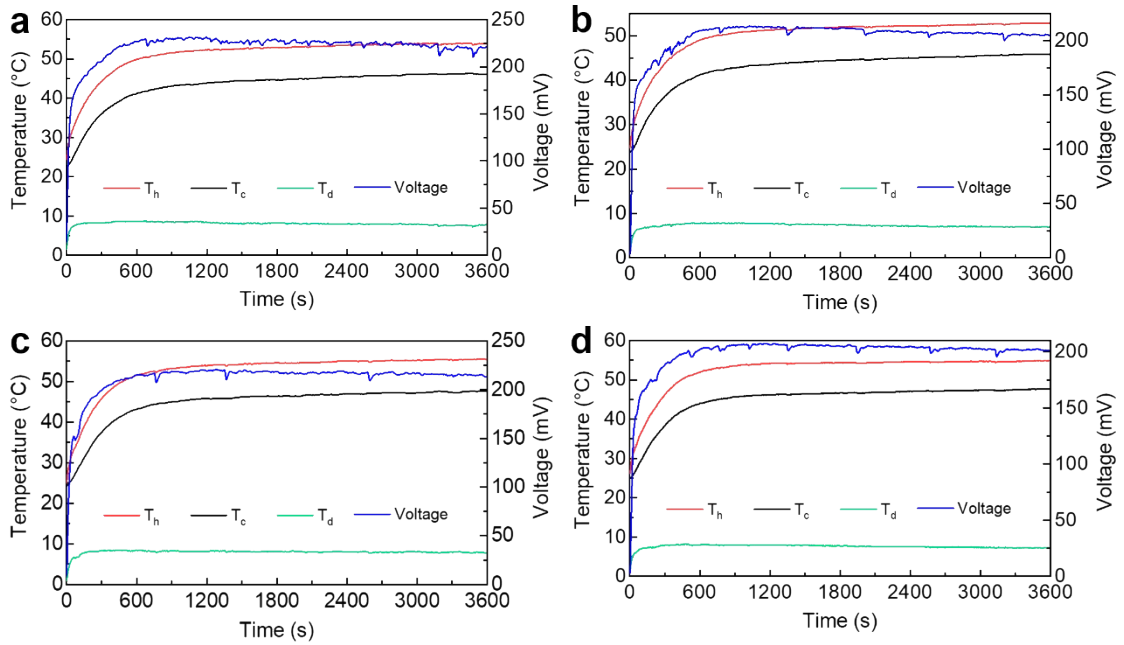

Fig. S16 The changes in T_h, T_c, T_d, and V_{oc} during water collection by A5.5–ACPFG in NaCl solutions of different concentrations under 1.0 sun for 1 hour. (a) Pure water, (b) 3.5 wt%, (c) 10 wt%, and (d) 20 wt%.

S2.16 The thermoelectric output of A5.5–ACPFG during water collection in sea salt solutions

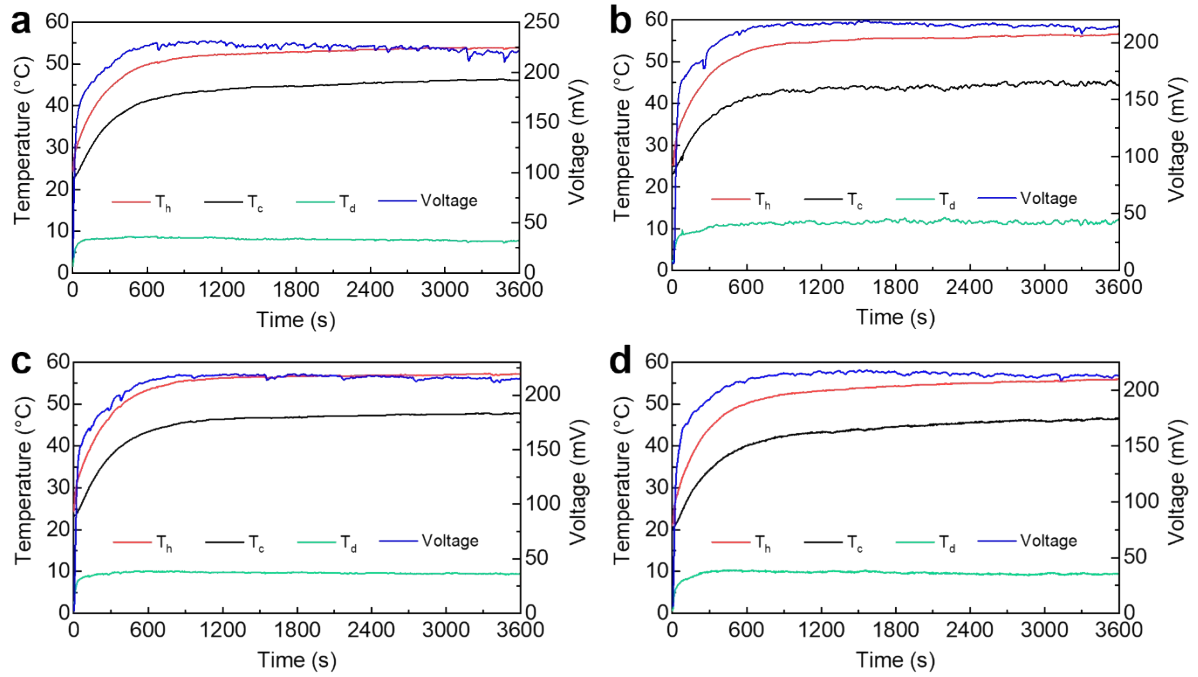

Fig. S17 The changes in T_h, T_c, T_d, and V_{oc} during water collection by A5.5–ACPFG in sea salt solutions of different concentrations under 1.0 sun for 1 hour. (a) Pure water, (b) 3.5 wt%, (c) 10 wt%, and (d) 20 wt%.

S2.17 The thermoelectric output of A13–ACPFG during water collection in NaCl solutions

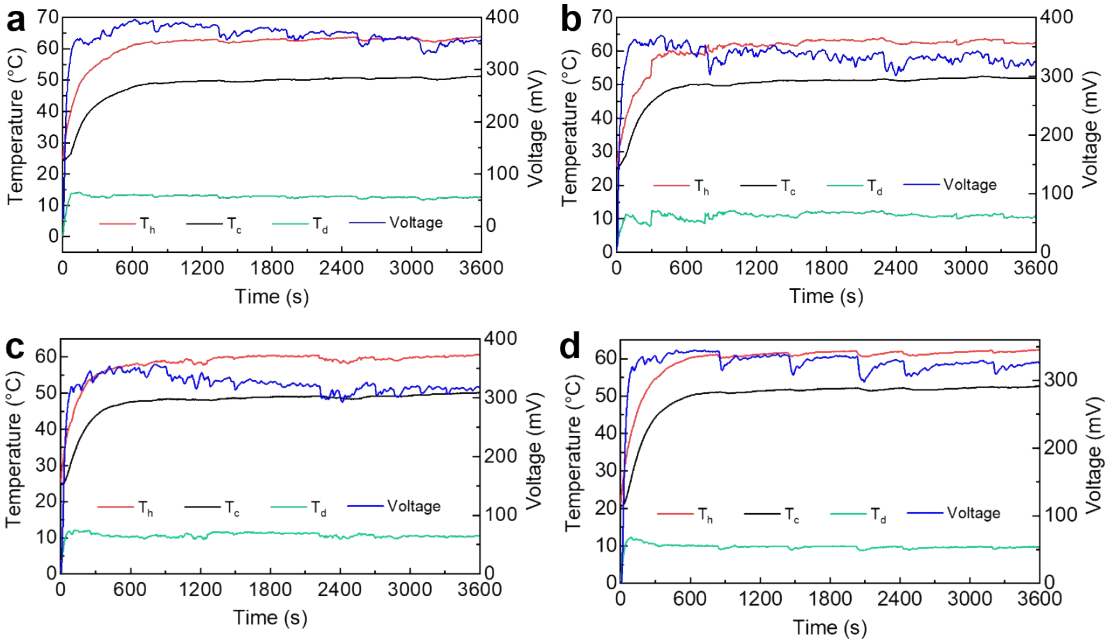

Fig. S18 The changes in T_h, T_c, T_d, and V_{oc} during water collection by A13–ACPFG in NaCl solutions of different concentrations under 1.0 sun for 1 hour. (a) Pure water, (b) 3.5 wt%, (c) 10 wt%, and (d) 20 wt%.

S2.18 The thermoelectric output of A13–ACPFG during water collection in sea salt solutions

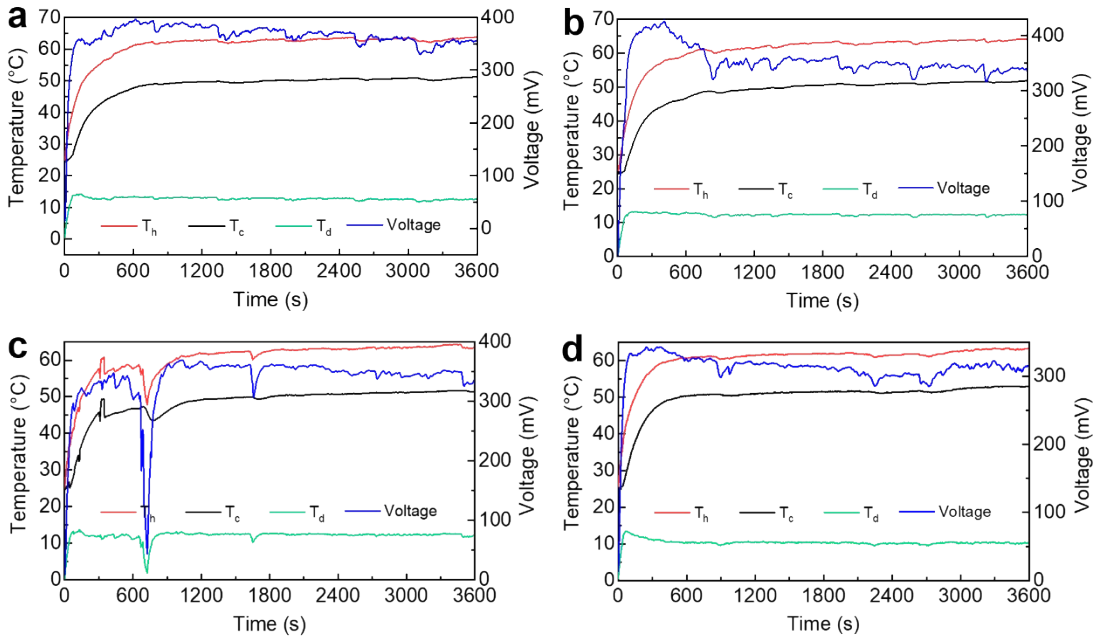

Fig. S19 The changes in T_h, T_c, T_d, and V_{oc} during water collection by A13–ACPFG in sea salt solutions of different concentrations under 1.0 sun for 1 hour. (a) Pure water, (b) 3.5 wt%, (c) 10 wt%, and (d) 20 wt%.

S2.19 The water collection of A5.5–ACPFG and A13–ACPFG

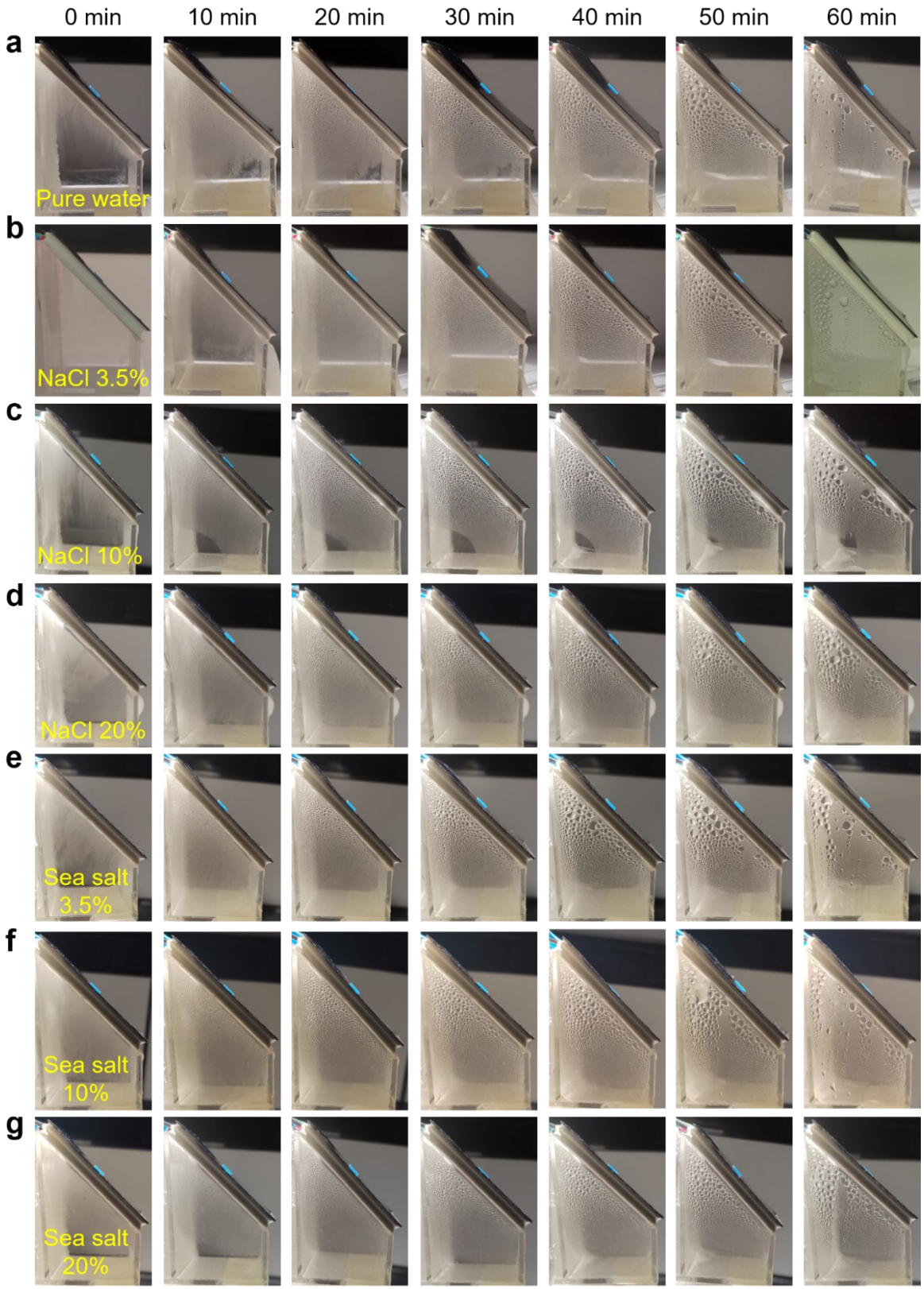

Fig. S20 Water collection situation of A5.5–ACPFG in salt solutions of different concentrations under 1.0 sun for 1 hour, including time periods of 0, 10, 20, 30, 40, 50, and 60 min. (a) Pure

water, (b) NaCl 3.5 wt%, (c) NaCl 10 wt%, (d) NaCl 20 wt%, (e) Sea salt 3.5 wt%, (f) Sea salt 10 wt%, and (g) Sea salt 20 wt%.

Fig. S21 Water collection situation of A13–ACPFG in salt solutions of different concentrations under 1.0 sun for 1 hour, including time periods of 0, 10, 20, 30, 40, 50, and 60 min. (a) Pure water, (b) NaCl 3.5 wt%, (c) NaCl 10 wt%, (d) NaCl 20 wt%, (e) Sea salt 3.5 wt%, (f) Sea salt 10 wt%, and (g) Sea salt 20 wt%.

S2.20 Salt resistance of ACPFG

During the 16-hour water collection process in A13, we found that salt mainly appeared outside the water collection chamber in contact with TEG, as shown in Fig. S22 and Video S1. It is worth noting that no salt crystallization phenomenon was observed on the evaporation surface or other areas. Moreover, the formed salt scale can be easily removed by a scraper. This good anti salt sedimentation effect is mainly due to two key factors. Firstly, TEG adopts a 45 ° inclined placement, which allows salt to move in a specific direction under the action of gravity during water flow, avoiding accumulation at the bottom of TEG. Secondly, CAT has excellent water transport capabilities, which can efficiently guide water flow and further reduce the possibility of salt deposition at the bottom of TEG.

In summary, the experimental results indicate that ACPFG can effectively prevent salt deposition at the bottom of TEG during seawater desalination, thereby ensuring long-term stable operation of the equipment and maintaining good performance.

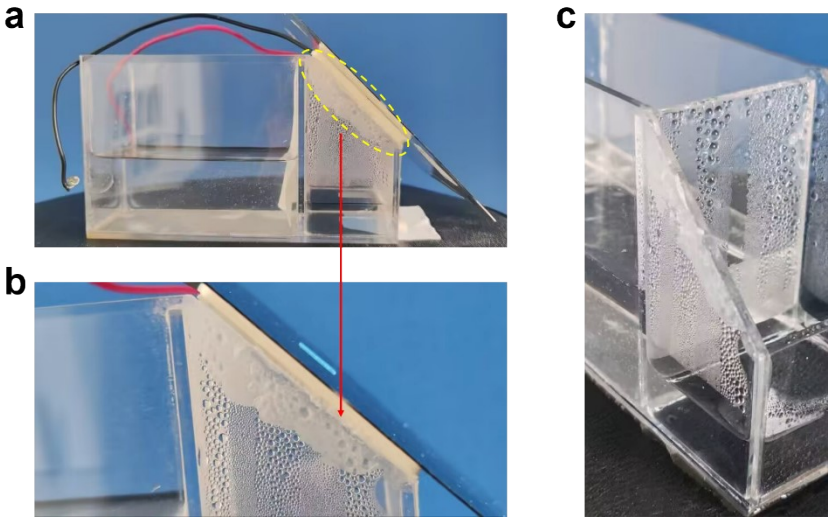

Fig. S22 (a) Salt precipitation of A13-ACPFG in a 10 wt% sea salt solution after 16 hours of water collection under 1.0 sun. (b) The photo of salt that mainly appears in outside the water collection chamber in contact with TEG. (c) No salt on the side of the water collection chamber.

S2.21 All-day electricity generation of ACPFG without water collection

Five ACPFG units (two A5.5s and one A7.5, one A10, and one A13 each) were used without collecting water and relying solely on evaporation cooling through PFW (Fig. S23). When measuring the open circuit voltage after series connection, the cold and hot junction temperatures of A5.5, A7.5, A10, and A13 were also measured separately. It is found that the cold junction temperatures of A5.5, A7.5, A10, and A13 can reach 34.8, 38.1, 45.2, and 48.5 ℃ during the day, and 24.4, 25.8, 26.3, and 26.8 ℃ at night; The hot end temperature can reach 45.8, 53.4, 60.3, and 65.4 ℃ during the day, and 25.5, 27.1, 28.3, and 28.7 ℃ at night.

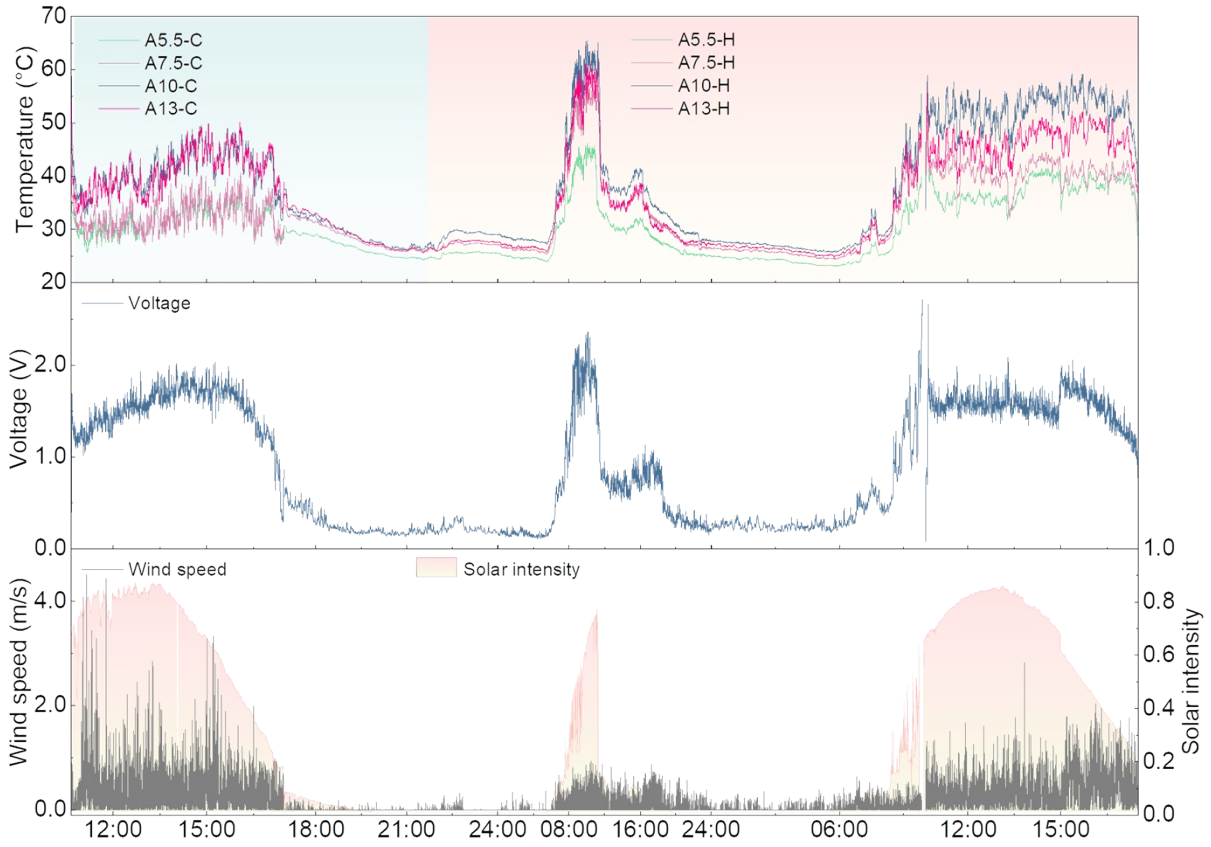

Fig. S23 The five ACPFG units connected in series without collecting water and relying solely on natural flowing water evaporation for cooling outdoors, their temperature of the hot and cold ends, V_{oc}, and corresponding solar intensity and wind speed throughout the day.

S2.22 Night-time operating mechanism

In order to elucidate the operational mechanism of ACPFG system at night, we have investigated the thermal profile distribution of the TEG during the nighttime operation of the ACPFG system through multi-physics field simulation (Fig. S24). Simulation results indicate that both A5.5 and A13 exhibit a gradient characterized by "cold end (water flow side) low temperature (blue) to hot end (ambient side) high temperature (red/yellow), with the cold-end temperature gradually increasing from the water inlet at the top downwards". This demonstrates that when the TEG hot end (integrated LEA side) is consistent with the ambient temperature at night, the continuous evaporation cooling of flowing water at the cold end constantly removes heat, causing the cold-end temperature to be significantly lower than the hot-end (ambient) temperature. This breaks the thermal equilibrium, driving heat conduction from the hot end (LEA, the ambient temperature) to the cold end (low-temperature water flow). Finally, the system reaches a dynamic steady state: the passive water flow continuously consumes cold-end heat to maintain low temperature, while the ambient continuously replenishes heat to the hot end through thermal radiation, maintaining hot-end temperature close to ambient temperature. Consequently, a stable temperature gradient forms and is maintained within the TEG, ranging from the cold end (blue, low temperature) to the hot end (red/yellow, high temperature).

Additionally, it was found that A5.5 has a longer cold-side low-temperature zone coverage, while A13 has a relatively higher hot-end temperature. This stems from the efficiency of heat acquisition from the environment at the hot end. For A5.5, the LEA area matches the TEG area, meaning the LEA is small, resulting in a small thermal exchange area and slow ambient heat replenishment. The heat supply fails to match the conduction consumption towards the cold end, causing the high-temperature zone to concentrate only at the tip of the hot end. For A13, the LEA-to-TEG area ratio reaches 5.6:1. The larger thermal exchange interface significantly enhances the ambient heat replenishment rate, leading to a large thermal

exchange area and fast ambient heat replenishment. Therefore, heat can be replenished more uniformly across the entire hot-end region, effectively resisting water-flow cooling, resulting in longer high-temperature zone coverage and a larger ΔT between the cold and hot end.

Therefore, the simulation results confirm that the ACPFG system utilizes a heat transfer chain including the evaporative cooling of passive water flow at the cold end, internal heat conduction within the TEG, and heat radiation between the LEA at the hot end and the environment, successfully establishing and maintaining a stable thermal gradient distribution within the TEG at night to drive power generation. They also show that the expansion of the LEA area at the hot end can improve the efficiency of environmental heat exchange at night.

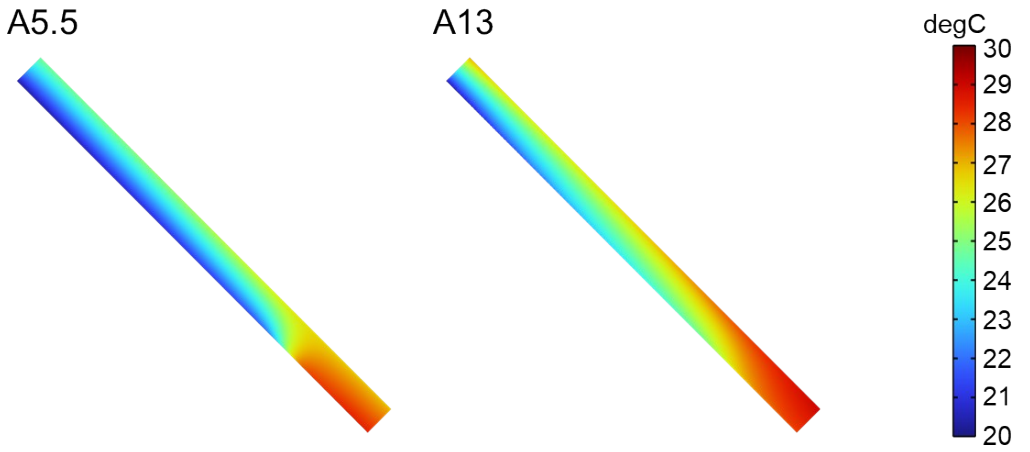

Fig. S24 The thermal profile distribution of the TEG during the nighttime operation of the ACPFG system through multi-physics field simulation.

S2.23 All-day electricity generation of ACPFG with water collection

When the open circuit voltage of collecting water was measured for five ACPFGs (two A5.5s and one A7.5, A10, and A13 each) after series connection, the cold and hot temperatures of A5.5, A7.5, A10, and A13 were also measured, as well as the cold and hot temperatures of A5.5 and A13–ACPFG (Fig. S25). It is found that the daytime hot and cold temperatures of A5.5 are 53.1 and 59 ℃, respectively, with a temperature difference of 6 ℃. The nighttime hot and cold temperatures are 26.5 and 27.9 ℃, respectively, with a temperature difference of 1.4 ℃; The cold and hot temperatures of A13 are 61.5 and 76.2 ℃, respectively, with a temperature difference of 14.7 ℃. The cold and hot temperatures at night are 27.7 and 28.2 ℃, respectively, with a temperature difference of 0.5 ℃.

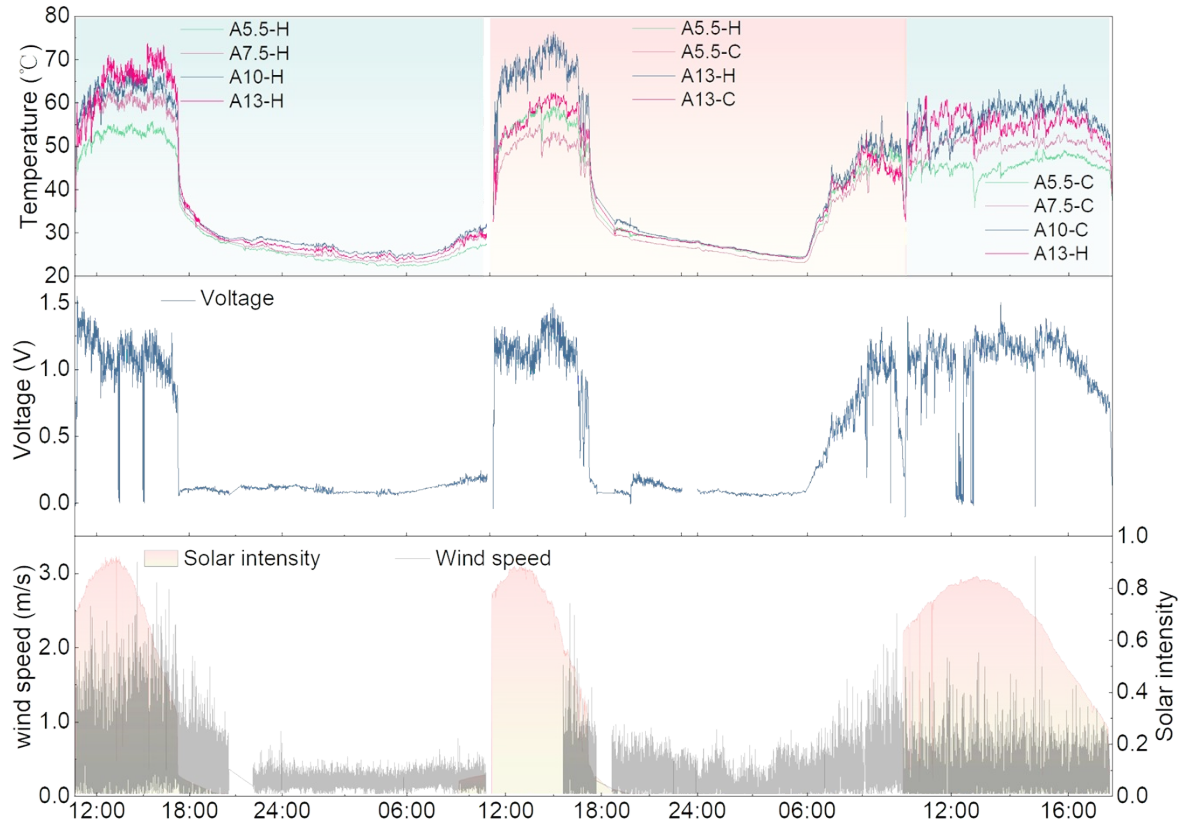

Fig. S25 The temperature of the hot and cold ends, V_{oc}, and corresponding solar intensity and wind speed of 5 series connected ACPFG units during water collection throughout the day outdoors.

S2.24 The V_{oc} of single ACPFG with and without water collection

The V_{oc} of individual A5.5, A7.5, A10, and A13–ACPFG was measured. Due to the effects of outdoor weather, wind speed and other conditions that change from time to time, their V_{oc} fluctuates within a certain range. The result is that when relying solely on water evaporation cooling without collecting water outdoors (Fig. S26), the minimum V_{oc} of A5.5, A7.5, A10, and A13–ACPFG are 0.335, 0.392, 0.445, and 0.488 V, respectively; and the maximum V_{oc} reach 0.393, 0.464, 0.476, and 0.544 V. When further collecting water (Fig. S27), the minimum V_{oc} of A5.5, A7.5, A10, and A13–ACPFG are 0.195, 0.220, 0.335, and 0.352 V, respectively; and the maximum V_{oc} reach 0.201, 0.258, 0.352, and 0.415 V.

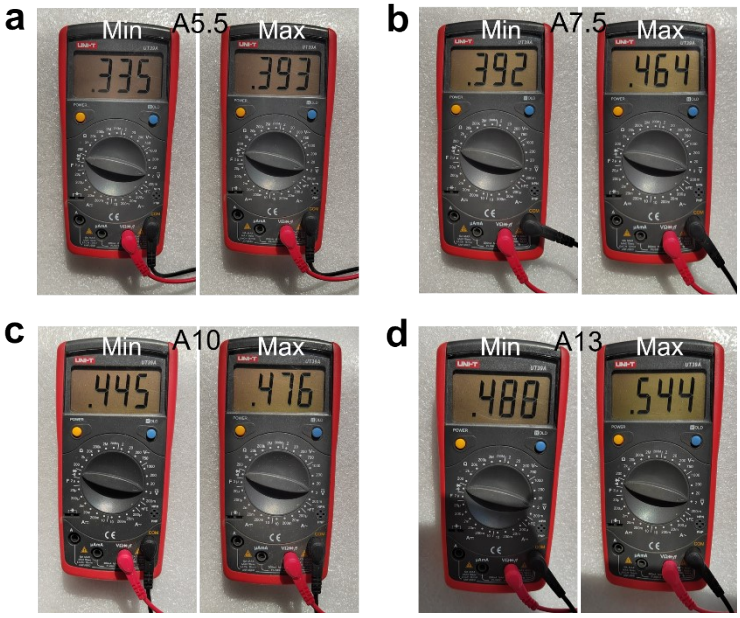

Fig. S26 The minimum and maximum V_{oc} of individual (a) A5.5, (b) A7.5, (c) A10, and (d) A13–ACPFG when relying solely on flowing water evaporation cooling but not collecting water outdoors.

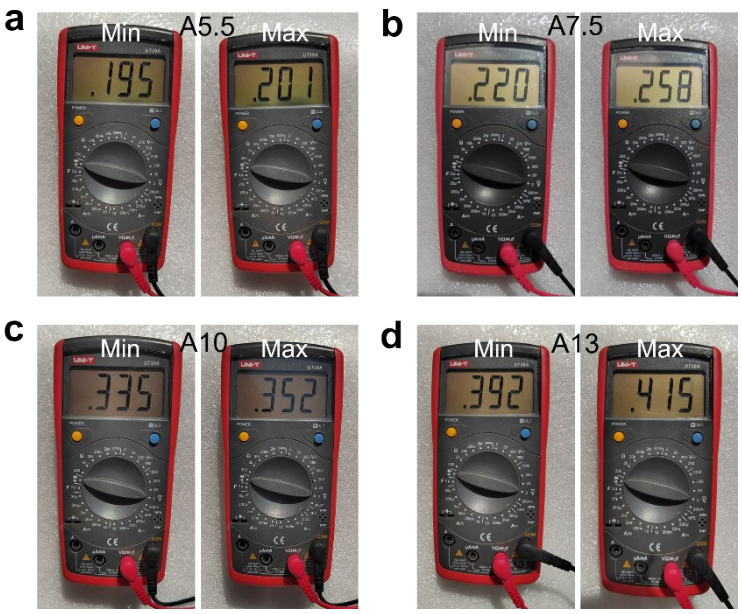

Fig. S27 The minimum and maximum V_{oc} of individual (a) A5.5, (b) A7.5, (c) A10, and (d) A13–ACPFG when collecting water outdoors.

S2.25 The thermoelectric output and water collection of ACPFG during water collection outdoors

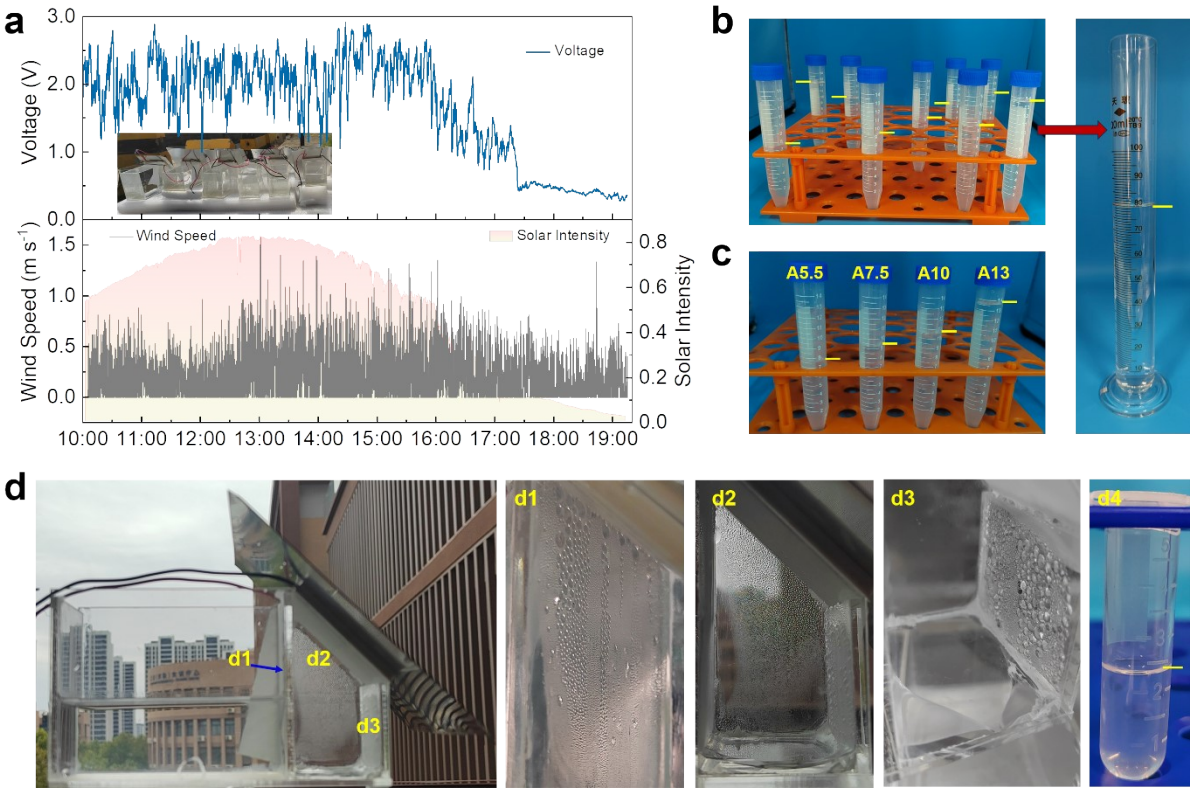

Fig. S28 (a) The V_{oc} and corresponding solar intensity and wind speed of 9 series connected ACPFG units during water collection in a simulated 3.5 wt% sea salt solution outdoors. The amount of water collected by (b) each ACPFG unit throughout the day, as well as that collected by (c) each A5.5, A7.5, A10, and A13–ACPFG. (d) Water collection capacity test of ACPFG under non illuminated conditions (overnight test). And the photos of dense water droplets on the side walls of the collection chamber and the total amount of water collected.

Section 3. Supplementary Table

Table S6 The detailed heat flux in ACPFG

	Unit	A5.5	A7.5	A10	A13
S_{LEA}	m^2	0.003025	0.006375	0.012	0.0169
S_{TEG}	m^2	0.003025	0.003025	0.003025	0.003025
$S_{LEA'}$	m^2	0	0.00335	0.008975	0.013875
P_{solar}	W	3.025	6.375	12	16.9
$P'_{r,LEA'}$	W	0	0.000268	0.000718	0.00111
$P'_{rad,LEA'}$	W	0	0.02403695	0.100018928	0.211261548
$P'_{conv,\ LEA'}$	W	0	0.169175	0.6865875	1.41525
P_{input}	W	3.025	6.18152005	11.21267557	15.27237845
$P_{r,LEA}$	W	0.242	0.509732	0.959282	1.35089
T_h	K	319.05	320.25	325.45	330.55
$P_{rad,h}$	W	0.019016101	0.02170501	0.033711115	0.046058824
$P_{conv,h}$	W	0.1346125	0.1527625	0.2314125	0.30855
P_h	W	0.153628601	0.17446751	0.265123615	0.354608824
T_c	K	310.05	310.55	314.65	316.65
$P_{rad,\ c}$	W	–0.001432095	0.00574225	0.065892288	0.096100026
$P_{conv,c}$	W	–0.0015125	0.00605	0.0680625	0.0983125
P_c	W	–0.002944595	0.01179225	0.133954788	0.194412526
P_{out}	$W\ m^{-2}$	0.562	0.772	1.17	1.837
P_e	W	0.00170005	0.0023353	0.00353925	0.005556925
P_l	W	0.394384056	0.69832705	1.361899653	1.905468275
η		86.96%	88.70%	87.85%	87.52%

References

1 V. Rinnerbauer, A. Lenert, D. M. Bierman, Y. X. Yeng, W. R. Chan, R. D. Geil, J. J. Senkevich, J. D. Joannopoulos, E. N. Wang, M. Soljačić and I. Celanovic, *Adv. Energy Mater.*, 2014, **4**, 1400334.

2 X. Wang, J. Zeng, X. Yu, C. Liang and Y. Zhang, *Appl. Surf. Sci.*, 2019, **465**, 986–994.

3 T. Li, M. Wu, J. Xu, R. Du, T. Yan, P. Wang, Z. Bai, R. Wang and S. Wang, *Nat. Commun.*, 2022, **13**, 6771.

4 B. Jin, Y. Lu, X. Zhang, X. Zhang, D. Li, Q. Liu, B. Deng and H. Li, *Chemical Engineering Journal*, 2023, **469**, 143906.

5 L. Chen, J. Ren, J. Gong, J. Qu and R. Niu, *Chem. Eng. J*, 2023, **454**, 140383.

6 X. Mu, J. Zhou, P. Wang, H. Chen, T. Yang, S. Chen, L. Miao and T. Mori, *Energy Environ. Sci.*, 2022, **15**, 3388–3399.

7 Q. Yan and M. G. Kanatzidis, *Nat. Mater.*, 2022, **21**, 503–513.

8 L. Wang, R. Moshwan, N. Yuan, Z.-G. Chen and X.-L. Shi, *Adv. Mater.*, 2025, **37**, 2418280.

9 G. Li, Y. Fan, Q. Li, Y. Zheng, D. Zhao, S. Wang, S. Dong, W. Guo and Y. Tang, *Renew. Sustain. Energy Rev.*, 2025, **207**, 114897.

10 F. Cao, K. McEnaney, G. Chen and Z. Ren, *Energy Environ. Sci.*, 2014, **7**, 1615–1627.